COUPLED DYNAMICS OF PARTICLES AND FLUID-FLUID INTERFACES

A Dissertation

by

YUN CHEN

Submitted to the Office of Graduate and Professional Studies of
Texas A&M University
in partial fulfillment of the requirements for the degree of

DOCTOR OF PHILOSOPHY

Chair of Committee,	Sungyon Lee
Committee Members,	Eric Petersen
	Jonathan Felts
	Prabir Daripa
Head of Department,	Andreas Polycarpou

December 2017

Major Subject: Mechanical Engineering

ABSTRACT

The study of the interaction between particles and fluid-fluid interfaces is essential to a variety of applications. A systematic way to understand those phenomena is to consider them in two different limits: single particle versus multiple particles. One particular example of a single particle problem is the particle's interaction with an acoustic bubble. Many bubble-based systems use oscillating microbubbles to trap particles, which further leads to applications including live animal trapping and cell manipulation. On the other hand, when multiple particles are involved, the study of the suspension injection and drainage has drawn much attention, which has the implication in biotechnology and food processing.

The objective of this research is to study and gain a fundamental understanding of the coupled dynamics between particles and fluid-fluid interfaces via experimental and theoretical approaches. First, we work on a project with a single-particle trapping via acoustic bubble. In this work, we quantify the magnitudes of secondary radiation force exerted by the oscillating bubble inside a microchannel for varying actuation frequencies and voltages. By combining well-developed theories that connect bubble oscillation yielding secondary radiation force to the acoustic actuation, we derive the expression to predict the critical input voltage that leads to particle release into the flow, which agrees with the experimental results.

The next phase of the research emphasizes the dynamics of the collection of particles. We experimentally investigate the effect of particle concentration on the viscous fingering behavior when the suspension is withdrawn from a Hele-Shaw cell. In particular, we quantify the fingering growth rate with varying initial particle concentrations. Our results reveal that the fingering growth rate increases with increasing particle concentrations,

while the total drainage time also appears to be increasing. This successfully proves that the drainage efficiency is enhanced due to the presence of the particles. In addition, we observe the particles entrained into the thin film on the plate after drainage, which also varies with the particle concentration and the ratio between gap thickness and particle diameter. Using a simplified model, we also find an entrainment criterion in agreement with the experimental results.

DEDICATION

To my advisor, Dr. Sungyon Lee, thank you for your guidance and patience throughout my PhD journey. Without your support and advice, this dissertation could not have been accomplished.

To my wife, Zhengyu, thank you for everything you have done, for all of your love and support. To my mother, Qiumei, thank your for providing me the opportunities to attend my graduate programs. To my father, Wenjiang, thank you for all those valuable suggestions and help through my life.

ACKNOWLEDGMENTS

I wish to express my thanks and gratitude for those who have supported and guided me to this successful work.

I would like to thank all my committee members: Dr. Eric Petersen, Dr. Jonathan Felts, Dr. Prabir Daripa for serving on my dissertation committee and providing me with all the valuable comments and suggestions for my research.

My thanks extend to all those who have given me helpful advice in those projects. In particular, I would like to thank Dr. Sascha Hilgenfeldt, Dr. Jungchul Kim, Dr. Jie Xu for fruitful discussions and Dr. Tony Yu for help with image processing. Also, I wish to thank Dr. Irmgard Bischofberger for her helpful feedback on the manuscript.

My sincere appreciation is offered to all my colleagues and those who have worked with me, particularly to Feng Xu, Alireza Hooshanginejad and Pedram Tazraei for your constant support and help in our lab. Special thanks to Frank Malambri, Francisco Falcon, Baylor Fain, Dillon Strack, Samuel Sweetin for providing great help for my research.

I would also like to thank Zecong Fang and Brett Merritt for being so helpful as our collaborator.

CONTRIBUTORS AND FUNDING SOURCES

Contributors

This work was supported by a dissertation committee consisting of advisor and committee chair Professor Sungyon Lee, and committee members Professor Eric Petersen, Professor Jonathan Felts of the Department of Mechanical Engineering, and Professor Prabir Daripa of the Department of Mathematics.

The experimental setup for Chapter 2, Section 2.2.1 were conducted by Zecong Fang at Washington State University.

All other work conducted for the dissertation was completed by the student independently.

Funding Sources

Graduate study was supported by Texas A&M Engineering Experiment Station (TEES).

TABLE OF CONTENTS

Page

LIST OF FIGURES

FIGURE Page

1. INTRODUCTION*

1.1 Background

The interaction between particles and fluid-fluid interfaces is observed in many situations, such as the balls bouncing on water, surface coating process, food production, mineral flotation and 3D printing. In the case of a single particle impacting the fluid-fluid interface, Lee et al.[1] experimentally show a superhydrophobic ball bounces off a free surface when it impacts with water, just as it impacts with an elastic membrane. They construct scaling laws to find conditions under which the particle sinks, bounces off or oscillates, which is relevant to water-walking insects and self-assembly using capillary forces. Another problem by Poulain et al. [2] is to experimentally characterize the dynamics of a spherical particle due to a cavitation bubble. Theoretically, they show that the particle velocity strongly depends on the distance from the bubble as an inverse-fourth power law. Also, Zhang et al.[3] experimentally study the collision of a single bubble with a fixed particle inside a Hele-Shaw cell for different initial transverse distances between the bubble and the particle. They develop a theoretical model to predict the rate of bubble volume shift from the smaller to the larger side. This topic is of importance in some industrial applications such as the mineral floatation which is related to the collision, attachment, and detachment of particles with bubbles in a suspension.

For multiple particles cases, Lubbers et al. [4] experimentally and numerically investigate the rapidly expanding monolayer by the impact of dense suspension drop on a solid surface. The results show that the expansion and the development of the spatial inhomogeneity are dominated by particle inertia, which is insensitive to the surface wetting,

*Part of this chapter is reprinted with permission from "Manipulation of Biological Objects Using Acoustic Bubbles: A Review" by Yun Chen, Sungyon Lee, 2014, Integrative and Comparative Biology, vol. 54, pp. 959-968, Copyright[2017] by Oxford University Press.

capillarity, and viscous drag. This result is a desired outcome in various coating processes such as thermal spray coating of sintered powders and additive manufacturing using inkjet printing. In a different context, Trojer et al.[5] experimentally study the effect of wettability on the fluid-fluid-displacement patterns in granular media. Their results demonstrate that increasing contact angle stabilizes the fluid invasion into the granular pack, and they also observe a stable radial displacement at low capillary numbers. Understanding and controlling the fluid-fluid displacement is essential in many applications, such as enhanced oil recovery, shale gas production, geological CO_2 storage and water infiltration in the soil.

There are many interesting research topics regarding the interaction between particles and fluid-fluid interfaces, and most of them are significant in various industrial applications and manufacture processes. The objective of this Ph.D. is to gain fundamental understanding of coupled dynamics between particles and fluid-fluid interfaces, via experiments and reduced mathematical modeling. In order to achieve this goal, two research projects have been studied. First, for a single particle case, we study the quantification of oscillation bubble for particle trapping. For multiple particles, we experimentally investigate the viscous fingering in a draining suspension.

1.2 Literature Review

1.2.1 Studies on Manipulation of Biological Objects Using Acoustic Bubble

In recent years, researchers have developed various applications in biology and medicine that utilize oscillating bubbles. The applications can be divided into three major categories: manipulation of microorganisms, deformation and rupture of cells/vesicles, and the delivery of drugs and genes.

1.2.1.1 Manipulation of Microorganisms

The first primary areas of development in lab-on-a-chip devices using acoustic bubble is the efficient manipulation of biological objects [6]. Researchers focus specifically on

microfluidic devices that utilize acoustic bubbles for manipulation. For instance, Xu et al. (2013) [7] perform experiments to capture and manipulate *C. elegans* using arrays of acoustic-driven oscillating microbubbles in a microfluidic device. As *C. elegans* have a simple, yet fully mapped, neuronal system, they are useful in studying various diseases. The size of bubbles are around $250\,\mu\mathrm{m}$. The input voltage is adjusted to accommodate different sizes of *C. elegans* . The selective capture and release of *C. elegans* depending on the acoustic input allow for sorting of worms by size as well as for controlling their swimming path by the timed actuation of the acoustic source [8, 9].

Acoustic bubbles are also employed to control other types of microorganisms, such as fish eggs and water fleas. Bubbles are first held stationary on hydrophobic plates and undergo oscillations upon acoustic actuation inside the microchip. The resultant secondary radiation force of the oscillating bubble leads to the capture of fish eggs and water fleas on the bubble's surface. Once the acoustic actuation is shut off, the microorganisms are released from the bubble. In the case of mobile water flea, they simply swim away upon release. For fish eggs, bubbles are placed on modular plates of which hydrophobicity is controlled by electrodes. The electro-wetting electrodes are connected to an independent voltage source and change the plate's property from hydrophobic to hydrophilic upon actuation. Subsequently, the bubble moves in the gradient of hydrophobicity, transporting the attached fish egg in the process.

Another application in the manipulation of micro-organism is to fragment $E.Coli$ of $4-6\,\mu\mathrm{m}$ in length by using acoustic bubbles [10]. $Escherichia\ Coli$ is widely used in screening cDNA genomic libraries for micro-scale analysis in biology [11]. Thus, the fragmentation of the $E.Coli$ will result in the release of intracellular protein and genomic DNA which can subsequently be harvested for biological research. Using the method of oscillating bubbles, the acoustic energy can be applied to a small sample volume without any chemical reagents or direct contact between the transducer and sample, which prevents

cross-contamination. In the work by Tandiono et. al, $E.Coli$ are injected into the microchannel at a given volume fraction, and bubbles are generated from instability of the gas-liquid interface inside the channel. With the acoustic actuation at a frequency of 128.7 kHz and a voltage of 200 V, $E.Coli$ are fragmented due to shear stresses generated by the streaming flow around an oscillating bubble.

1.2.1.2 Deformation or Rupture of Cells/Vesicles

The second application of acoustic bubble is deformation or rupture of cells and vesicles. Cells are basic units of living organisms and hold extreme significance in biomedical research [12], whereas a vesicle enclosed by a lipid bilayer is useful in cell biology [13] and may be formed naturally or artificially. In some cases, the study of cell structure requires the given cell to be sheared and ruptured, also known as cell lysis. One method of lysing cells is to utilize shear stresses generated by microstreaming of an oscillating bubble, analogous to the fragmentation of $E.Coli$. This concept is first demonstrated by Hughes and Nyborg [14] who state that the shearing action of bubble-induced micro-streaming causes the breakage of cells. More recently, a single bubble (10-100 μm in radius) is attached and stabilized by capillary forces inside an indentation [15]. With the actuation of ultrasonic energy, a vesicle with a radius of 10 μm is alternately pulled toward and away from an oscillating bubble due to the streaming flow. The speed of the vesicle increases with the increasing acoustic amplitude. In particular, large vesicles remain in the stagnation line of the oscillating bubble and are deformed by shear stresses of the streaming flow. With an increase in the fluid's viscosity and driving amplitudes, the shear stresses become large enough to rupture the vesicles. Marmottant et al. [16] also conduct further experiments and develop theoretical models of the deformation of vesicles due to microstreaming.

Another example of cell lysis is the rupture of $Pichia\,Pastoris$ for harvesting and analyzing its intracellular contents [10]. $Pichia\,Pastoris$ is a species of yeast cell with

rigid extracellular cell wall, which provides structural strength to the cell and renders lysis of the cell difficult. In this work, the yeast cells ($4\,\mu\mathrm{m}$ in diameter) are injected into the microchannel, and the bubbles are generated from the gas liquid interface in the channel. Upon acoustic actuation, cells near bubbles are shown to initially undergo large deformations and eventually split into two fragments. The physical mechanism of this rupture of the cell is the presence of shear inside a streaming flow.

Other studies also successfully demonstrate deformation and rupture of cells by an oscillating bubble. Following the work of Hughes and Nyborg [14], Rooney [17] experimentally shows that the release of hemoglobin occurrs when the oscillation of the bubble's amplitude exceeds a critical value. He attribute the observed hemolysis to microstreaming generated by an acoustic bubble. Miller et al. [18] also experimentally demonstrate that the bubble's oscillation may induce the cell's lysis. Furthermore, van Wamel et al. [19] conduct experiments to find the critical shear stress generated by the oscillating bubble needed to rupture the bovine endothelial cell membrane.

More recently, several groups have improved and applied the acoustic bubble techniques for the rupture or sonoporation of cell membranes in more biological applications [20, 21, 22, 23, 24]. These studies build the theoretical and experimental basis for the effectiveness of acoustic bubbles in medical treatment. For instance, the study of vesicle rupture [15] may be extended to opening pores in cell membranes for delivering drugs [25]. However, although the theoretical framework for both cases remains the same, the direct application of results from microfluidic experiments to highly complex clinical studies remains a challenge, since the acoustic parameters uniquely depend on each experimental setup. Therefore, more experimental and theoretical studies of the acoustic bubble are needed to bridge the gap between "lab-on-a-chip“ level studies and $in\ vitro$ experiments.

1.2.1.3 Delivery of Drugs and Genes

As previously mentioned, acoustic bubbles can be applied to delivering drugs or genes for medical treatment [26, 27, 28]. In particular, employing acoustic bubbles has been shown to enhance the efficiency of delivering drugs in three distinct ways [29, 30]. First, streaming flows generated by the oscillating bubble may rupture drug-loaded carriers and release the drugs in a controlled way, without damaging the loaded drugs [25]. Second, shear stresses generated by the acoustic bubble can perforate blood vessels or cell membranes and render them permeable. During oscillations, the streaming flow will open pores or large holes in cells or blood vessels, facilitating the delivery of drugs to target locations [21]. This enhances the efficiency of delivering drugs in practical medical treatment [31, 25]. Finally, bubbles themselves are used as drug carriers and are delivered into blood vessels [32, 33, 34]. When the microbubbles are injected into blood vessels, the bubbles will oscillate and migrate under the acoustic excitation [35]. Therefore, if acoustic bubbles are used as drug or gene carriers themselves, they can be delivered to a target location more precisely by modifying the acoustic input parameters.

Alternatively, the bubbles can exert secondary radiation forces to capture the nearby drug carriers and transport them to a target location by another acoustic excitation [36]. Several groups have worked on the methods to load drugs on a bubble [37, 38, 39, 40, 41]. The advantage of using bubbles to carry drugs is that the contents can be released locally in the targeted area, while minimizing the effects in untreated body parts [42]. In addition, some biological drugs such as nucleic acids and proteins degrade rapidly after being injected into the blood vessel; therefore, binding of drugs onto the bubble prevents degradation. For instance, Negishi et al. [43] develop the method of delivering genes using acoustically actuated bubble-liposomes $in\,vitro$. The results show a more efficient gene expression in the tissue where the acoustic source is applied, after the bubble-liposomes

are injected into the knee joints of mice. Mullin et al. [29] also report similarly successful delivery of drugs by way of acoustic bubbles.

1.2.2 Studies on Fingering Phenomena during Drainage in Hele-Shaw Cell

1.2.2.1 Viscous Fingering in Pure Oil

Paterson[44] perform experiments to show that the fingering occurs when a more viscous fluid that is surrounded by a less viscous fluid in Hele-Shaw cell is withdrawn through a sink. In the experiment, more viscous liquid is first injected into the Hele-Shaw cell otherwise filled with less viscous liquid to achieve a circular interface and then is sucked out at constant flow rate. Two conditions are performed here: glycerine as the more viscous fluid while air or oil as the less viscous fluid. The result shows that fingers occur at the interface when liquid contracts, and eventually one finger dominates and accelerates into the sink. When air is used as the less viscous fluid, the withdrawal ceases soon after the air reaches the sink. However, if oil is used as less viscous fluid, the withdrawal continues after the finger reaches the sink so that more fingers will converge into the sink. A similar study is reported by Thomé et al. [45], in which they first perform the experiments using an angled cell and inject the air into the periphery of the cell filled with oil so that the fingering occurs as a convergent case. Due to the geometry of the cell, the finger become narrow as they grow. The interface can be empirically fitted with the solution from Saffman and Taylor [46]. Then they perform the experiment using a circular cell and inject oil into the air first. With hydrostatic pressure the oil is siphoned out of the cell, and several fingers are observed. The siphoning stops and all other fingers are motionless when the fastest finger reaches the center.

Viscous fingering also occurs when the top plate of Hele-Shaw cell is lifted at a constant speed. Lindner et al.[47] study both experimentally and numerically on silicone oil that is confined in the Hele-Shaw cell. The top plate of the cell is then lifted at a constant

speed, during which air fingers enter into the oil from the outside. When the fingers grow their number decreases, eventually retracting to a nearly circular shape. They compare the results from the experiment with simulation and show that the number of fingers is solely dependent on the surface tension, while the extent of finger growth depends not only on the surface tension but also on initial condition. Lindner et al.[48] extend their work to perform a linear instability analysis and predict the number of growing fingers which matches with the experiment. They also show the dependance of the lift force on the finger patterns. Amar et al.[49] perform a linear theory analysis of instability in the lifting Hele-Shaw cell. However, their results show significant difference between the theory and experiment; the number of fingers that is theoretically predicted is roughly an order of magnitude larger than the experimental results, which is due to the limited 2D model. Hence they take the 3D effects into account, which is found to improve the prediction and agreement with the experiment. More recently Pedro et al. [50] propose an analytical model in which the lift force is not only affected by fingering but also dependent on the viscous normal stresses and the action of the wetting film left behind on the plates of the lifting apparatus. They compare the results of their model to the experimental results by Lindner et al.[48] and show the improved prediction for the lift force.

Chen et al.[51, 52] perform the numerical simulations of both inward and outward radial flows in Hele-Shaw cell. The model for a suction driven flow in a Hele-Shaw cell uses constant gap width and viscosity ratio (more viscous for inner fluid and less viscous for outer fluid). In one recent numerical study[52], they start from Boussinesq Hele-Shaw-Cahn-Hilliard model[53, 54] and fix the Péclet (dissipation) and Cahn (dispersion) number to be $Pe = 10^3$ and $C = 10^{-5}$ while varying the capillary number to the order of $Ca \sim 10^3$. The solution shows that for an initially circular interface a larger number of fingers develops and more fingers are detected by increasing the capillary number. Fingers compete with each other when they grow and move toward the sink, and eventually

a longer finger reaches the core accompanied by other competing fingers. The numerical solution shows very similar phenomena as the experimental observation by Paterson and Thomé et al. However, due to the lack a of detailed quantification of the experiment results, the numerical solution cannot have a quantitatively comparison with the experiments. In addition, Chen et al. also perform simulation at a higher capillary number in the order of $Ca \sim 10^4$. The results show that the number of fingers increases, and nonlinear phenomena such as finger merging, shielding, and pinch-off are observed. However, no experiments have been performed at such high values of capillary numbers, hence there is no validation of these numerical results.

A hydrodynamic stability analysis has been studied by Daripa et al.[55, 56, 57, 58] on multilayer Hele-Shaw flows. In the set up, the Hele-Shaw flow consists of three layers of immiscible fluids with different viscosities in which the middle layer has a smooth viscous profile. Their work establishes the connection of the variable viscosity results to viscous fingering in a complex fluid. Following these work, Gin and Daripa [59, 60] perform a linear stability analysis of the thin film flows in a radial geometry with multiple layers of immiscible fluids. They are able to provide a stabilization criteria and design an almost stable multi-layer system. Some other numerical research[61] has been performed to study a circular drop or blob viscous fluid surrounded by less viscous fluid and is drawn into an eccentric point sink. Nie et al.[62] analytically and numerically study singularities in a Hele-Shaw cell driven by surface tension and suction from a sink. They construct various exact solutions for zero surface tension. In the numerical solution for nonzero surface tension case with different initial interfaces, long fingers are observed and move faster and faster before reaching the sink. They also extend their work for the flow driven by multipole for a 2D Hele-Shaw cell with surface tension[63]. In this work, they can predict the direction from which the interface travels toward the multipole and estimate the distance between the fingertip and multipole as a function of time. Kelly et al. [64] use a numerical

algorithm based on a boundary integral equation assuming inviscid surrounding fluid and a small, finite surface tension to solve for the behavior of narrow finger propagating towards the sink. Results show that the finger narrows when the surface tension coefficient decreases, but the shape of the finger does not depend on the offset of the sink. A similar numerical study is performed by Hector et al.[65] who show that with small or negligible viscosity of the surrounding fluid, the interface develops a finger that bulges and later evolves into a wedge when approaching the sink. A neck is formed at the top of the finger. However, using a surrounding fluid with larger viscosity can prevent the formation of the neck and leads to thinner fingers.

1.2.2.2 Viscous Fingering in Particulate System

Drainage problems can also be performed in porous media with particles. Maløy et al.[66] conduct the experiments where 1 mm beads are sandwiched between plastic sheets and water is withdrawn from one end of the channel. They find that the extraction of water at a constant rate does not lead to air replacing water from pores. Instead, the interface tends to move to narrow parts of throats between the pores. The pressure fluctuations they measure are in good agreement with the simulation results. This work is followed by their study [67] on the shape and structure of drained areas, which is caused by the competition between buoyancy and capillary effects. Løvoll et al.[68] extend this work both experimentally and numerically considering the effects of gravity, capillary, and viscous forces. Transition from a capillary fingering to a viscous fingering behavior is observed. They experimentally determine the threshold for the instability and use percolation theory to predict the scaling of the front width and the stabilization criterion. Their experimental results and theoretical prediction are all consistent with the numerical results. Toussaint et al. [69] study how the viscous fingering is affected by the pore-scale with a random porous medium. They find that when averaged over the quenched disorder in capillary thresholds,

the interface growth rate is proportional to the local pressure gradient with a power of two. Aursjø et al.[70] perform a quasi-two-dimensional drainage experiments and compare the results with a 2D Lattice Boltzmann simulation. The experiments and simulation consist of approximately 10×10 (2 mm in diameter) pores, and glycerol-water is withdrawn at a constant rate. They find that the only difference for the comparison between 2D LB simulation and the experiment is the small effect related to the three-dimensional topology of the experiments, which the 2D simulation could not predict. Otherwise, the simulation results have a good agreement with the experiments. Sandnes et al. [71] study patterns of the flow in a Hele-Shaw cell with varying grain concentration and amount of air injected. From their phase diagrams, they observe transition between various patterns depending on different parameters. They also define two regions: frictional regime and viscous regime, according to different injection flow rate, where they observe stick-slip bubbles and viscous fingers, respectively. More recently, Amina et al.[72] perform the experiments using a vertical placed Hele-Shaw cell filled with glass beads from 0.1 mm$\sim$0.7 mm in diameter saturated with water. They inject air from the bottom and observe the transition from capillary invasion to viscous fingering to fracturing. The fractal dimension numbers for these three different invasion patterns are also obtained from the experiments.

2. QUANTIFICATION OF PARTICLE TRAPPING VIA ACOUSTIC BUBBLE*

2.1 Introduction

In the past two decades, microfluidics technology has become an emerging field that allows for precise control of fluids behavior at microscale[73, 74]. Based on microfluidic technology, functional units, such as pumps, valves, sensors, and actuators, can be miniaturized and integrated onto a small microfluidic chip to form a lab on a chip system[75, 76], which is now finding numerous applications in chemistry[77], biology[78, 79, 80], medicine[81, 82], biotechnology[83], food science[84] and environmental engineering[85]. One of the most important functions in lab on a chip applications is the manipulation of micro-sized objects, including reagents, particles, cells, and microorganisms. Various methods have been developed for manipulation in a microfluidic environment. These methods often harness interactions between fluids and multi-physics, such as electric field[86, 87, 88, 89, 90, 91], magnetic field[92, 93, 94, 95], electromagnetic field[96, 97, 98], temperature field[99, 100] and centrifugal force field[101, 102]. In recent years, acoustics has also started to attract attention as an alternative source that can be utilized for manipulation of micro-objects in microfluidics, and a new term *acoustofluidics* has gained popularity in the research community[103, 104]. Compared with other actuation techniques, acoustic methods offer many advantages, such as versatility, compactness, non-contact feature and relatively simple operation. However, the interactions between fluids and an acoustic field can be quite complex; Fig. 2.1 briefly summarizes possible acoustic effects that may arise when acoustics and fluids encounter at microscale.

Two types of interactions have been explored in the past. One is to directly use the

*Reprinted with permission from "Onset of particle trapping and release via acoustic bubbles" by Yun Chen, Zecong Fang, Brett Merritt, Dillon Strack, Jie Xu and Sungyon Lee, 2016, Lab on a Chip, vol. 16, pp. 3024-3032, Copyright[2017] by Royal Society of Chemistry.

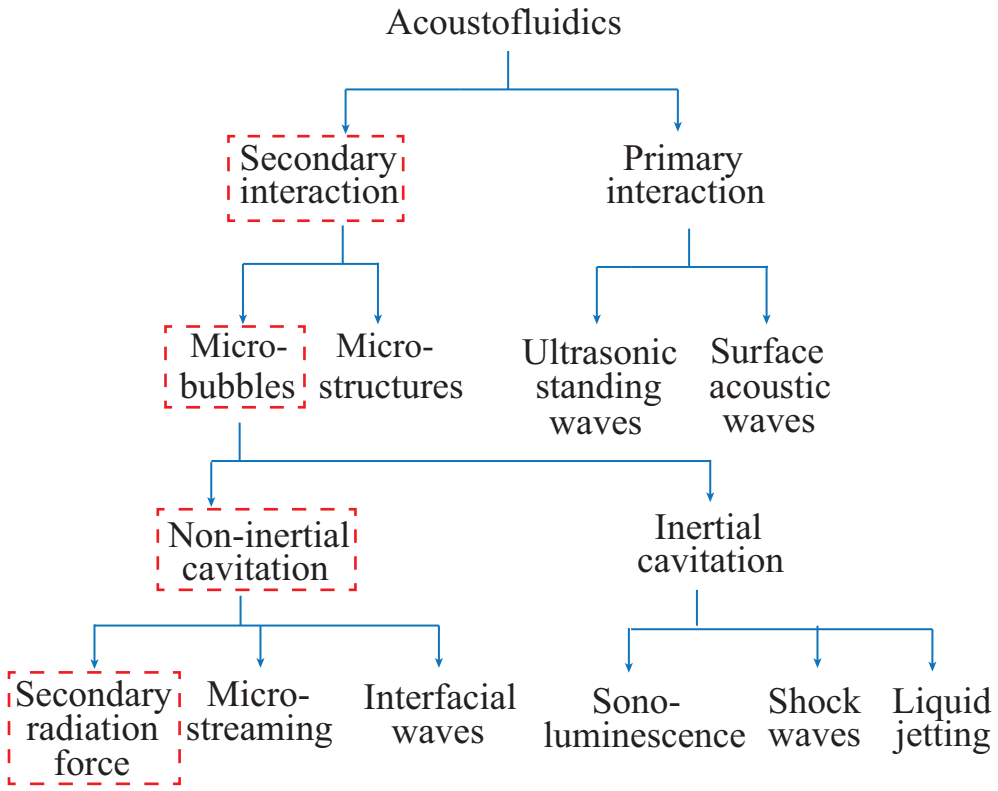

Figure 2.1: Diagram showing different interactions between acoustic actuation and fluid flows. The microbubble oscillation caused by acoustic field is in the secondary interaction category. The oscillating bubble can impact the objects in the nearby field generating microstreaming flows and secondary radiation forces, F_{SR}. In this study, we focus on the effect of F_{SR}.

interactions between objects and acoustic waves, which include surface waves[105, 106] or bulk standing waves[107, 108]. The other is to harness secondary acoustic effects in the vicinity of solid structures including microchambers[109] and sharp edges[110], or most often, microbubbles[111, 112]. In particular, microbubbles oscillating in an acoustic field can be categorized into inertial or non-inertial types depending on the oscillation magnitude. Inertial bubble oscillation, or inertial cavitation, is very violent, unstable, and transient, resulting in liquid jetting in the case of the asymmetrical bubble collapse, or energy emitting via shock waves or light[113]. This particular mode of acoustic bubbles has

been widely used in medical ultrasonics[114, 115, 116, 117]. Non-inertial microbubble oscillation is much gentler with various stable oscillation modes that may be observed in the form of interfacial waves[118, 119]. Non-inertial microbubbles may influence surrounding objects by generating microstreaming flows[120, 121, 122], or by exerting a secondary radiation force, F_{SR}[123, 124].

Most bubble-based lab on a chip systems to date utilize non-inertial microbubbles, due to the fact that non-inertial microbubbles are more stable and can be easily controlled both spatially and temporally in a microfluidic environment. For example, the secondary radiation force from an oscillating bubble can be used to trap micro-objects, while the position of the bubble itself can be controlled by using electrowetting technique[9] or simply attaching the bubble to a traverse rod[125]. If an array of bubbles is fixed inside a microchannel and acoustically actuated, a trapping zone will form near the oscillating bubbles, which can be used to enrich, sort and manipulate *C. elegans* in a flow[7]. Moreover, if excited with maximized microstreaming flows, spatially arranged bubbles in a microchannel can be used as fixated transporters[126, 127, 128, 129]. Other notable applications involving acoustic bubbles include enhanced mixing[130], pumping flow in a microchannel[131, 132], switching particle pathlines[133], switching flow optical properties[134], assembling and driving microrotors[135], generating chemical gradients[136] and propelling objects[137, 138].

Although applications of acoustic bubbles in lab on a chip systems have witnessed tremendous progress recently, the operating conditions of the experiments are largely determined empirically in most applications mentioned above, and there exists a lack of theoretical guidance for designing devices. Indeed, it has been shown that even for a simple straight 1D channel, the actual outcome of the acoustic actuation is difficult to predict using theoretical or numerical methods[139]. Therefore, for any given device, initial experimental validation is important for any further theoretical or modeling efforts. One

particular area of acoustofluidics with the latest theoretical development is microstreaming flows [140, 141, 142, 127, 143, 16, 144], as both the microstreaming flow field and its effect on micro-sized objects have been resolved analytically in two-dimensional and quasi-three dimensional geometries. By contrast, while the theoretical expression of F_{SR} has been developed by Nyborg [14] and Doinikov [145], it has not been experimentally verified or implemented to directly quantify the bubble's ability to trap a given micro-object in microfluidic devices. For instance, Xu et al [7] and Neild et al [146] demonstrated trapping of microworms and microspheres, respectively, via acoustically actuated bubbles that exert secondary radiation forces. However, no measurement of bubble oscillations has been made to connect the amplitude of bubble oscillations to F_{SR}, then to the ability of bubbles to trap particles. The authors also reported the critical voltages at a given frequency that lead to particle trapping but offered no quantitative analysis that connects the critical acoustic parameters to F_{SR}.

In order to address this current lack of quantitative analysis of F_{SR}, I hereby present the combined experimental and theoretical studies on particle trapping and release via an acoustic bubble in a simple 1D microfluidic channel. This will serve as an important first step towards more comprehensive future studies. Experimentally, I quantify the bubble's ability to stabilize a particle in two ways: first, by measuring the critical acoustic input at which a pre-loaded particle is released into the flow (Exp A); secondly, by measuring the critical acoustic voltage and frequency at which a particle is directed towards the bubble and is stabilized (Exp B). The corresponding amplitudes of bubble oscillations that give rise to F_{SR} are also measured. Furthermore, to isolate the effects of F_{SR} from all other forces acting on the particle, we keep the flow rate inside the channel constant to ensure that the relative effects of microstreaming flows may be neglected in our study. In addition, we combine the well-developed theories that connect bubble oscillations yielding F_{SR} to the acoustic actuation to theoretically derive the critical voltage.

Following the experimental method and image processing in Section 2.2, experimental results are reported in Section 2.3.1, consisting of the bubble oscillation magnitudes and the corresponding behavior of the microsphere at given voltages and frequencies. Sections 2.3.2 and 2.3.3 include the theoretical analysis to calculate the critical input voltage that leads to the particle release into the mean flow, in reasonable agreement with the experiments. The summary and future directions are given in Section 2.4.

2.2 Methods and Materials

2.2.1 Experimental Setup

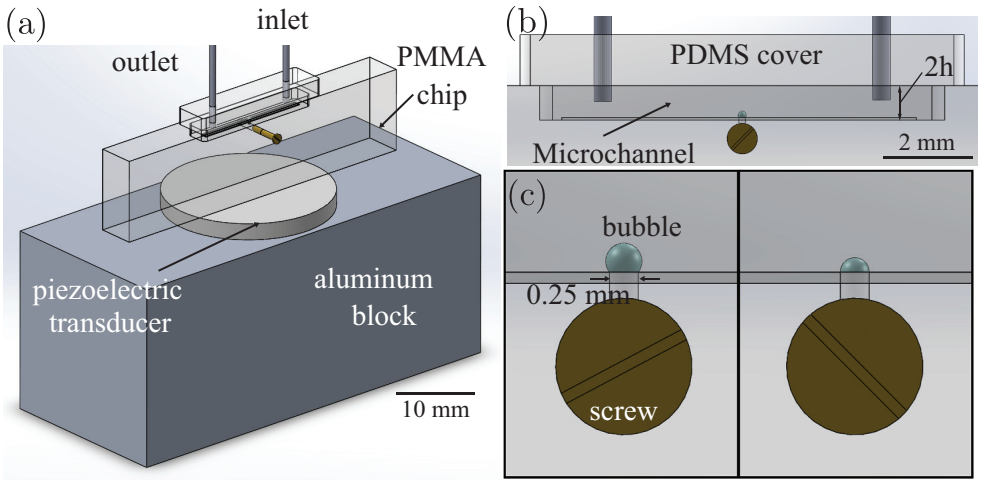

Figure 2.2: (a) The piezoelectric transducer is sandwiched between the microfluidics chip and aluminum block. (b) The microchannel is milled on top of the chip. (c) The size of the bubble is controlled by a screw.

The experiment is performed by our collaborator Fang from WSU. The experimental apparatus used in this study includes a transparent microfluidic chip, a piezoelectric transducer, and an aluminum block base, as shown in Fig. 2.2(a). The microfluidic channel (depth 2.79 mm $\times$ height 1.35 mm $\times$ length 14.01 mm) has been micro-milled out of

PMMA (Fig. 2.2(b)) and is sealed with PDMS and plastic sheets, with two flat needles (Lab Express Management) used as an inlet and an outlet. The channel also consists of a cylindrical cavity with diameter of 254 μm which is treated with superhydrophobic coating (Rain-X) to serve as a pre-defined site of bubble formation and stabilization[147]. An additional cylindrical cavity is drilled from the side to incorporate a miniature screw to actively control the bubble volume and is sealed by ultrasound gel (Aquasonic 100, Parker Laboratories), as shown in Fig. 2.2(c).

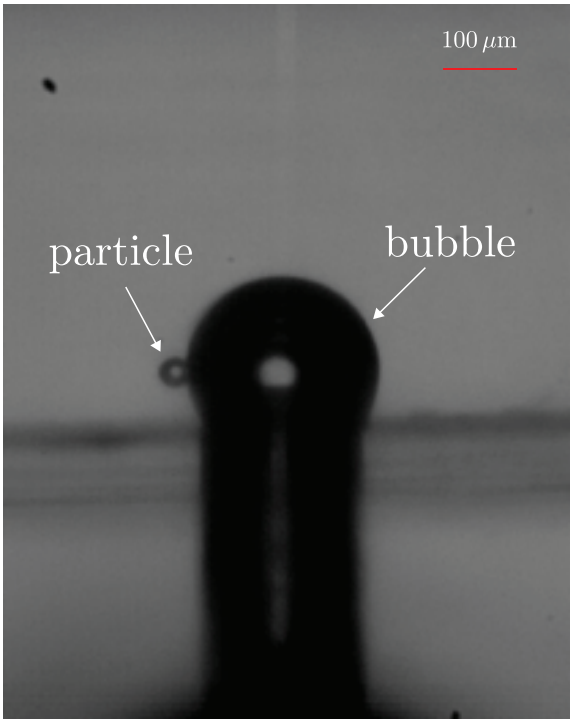

Figure 2.3: A particle is trapped by the oscillating bubble once the piezoelectric transducer is excited.

In our experiment setup, an air bubble forms automatically inside the cavity and remains stable when the solution with polystyrene microspheres (25-30 μm radius, Thermo Fisher Scientific) is introduced into the main channel through a syringe pump at a constant

flow rate of 4 mL/min (NE-1000, New Era Pump Systems) as shown in Fig. 2.3. Following the bubble formation, the screw is actively adjusted to achieve the desired bubble radius, typically in the range of 140 -160 μm. We use a piezoelectric transducer (20 mm $\times$ 2 mm) sandwiched between the PMMA chip and an aluminum block to excite the channel periodically using a function generator (DG1022, RIGOL Technologies) and an amplifier (7602M, Krohn-Hite). The driving frequency, f, ranges from 20 kHz to 36 kHz with an increment of 1 kHz, while the driving voltage, V, is varied from 10 V to 190 V at each frequency.

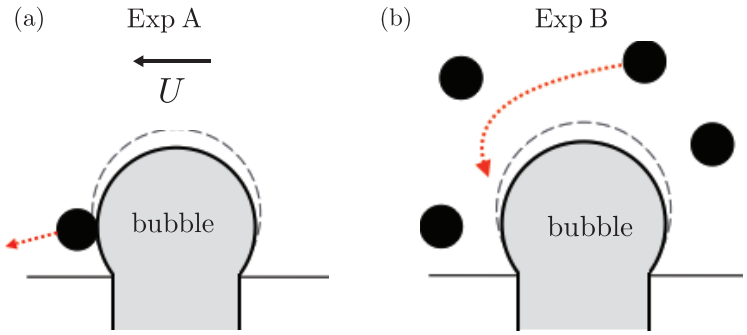

Figure 2.4: (a) In Exp A, the particle is first trapped on the surface of the bubble and then released. (b) In Exp B, the critical voltage, V_c, is recorded at which an acoustic bubble is able to trap the particle originally in motion for varying f.

An example of particle trapped by an oscillating bubble recorded by the camera is shown in Fig. 2.3. The particle suspension is flowing from the right to the left in the micro channel due to the external flow. Once the piezoelectric transducer is excited, the bubble starts oscillating. Those particles flowing near the bubble are trapped, usually at the stagnation point of the bubble.

Two sets of experiments are conducted to quantify threshold acoustic parameters for particle trapping and release, as depicted in Fig. 2.4 (a) and (b). In the first set (Exp A),

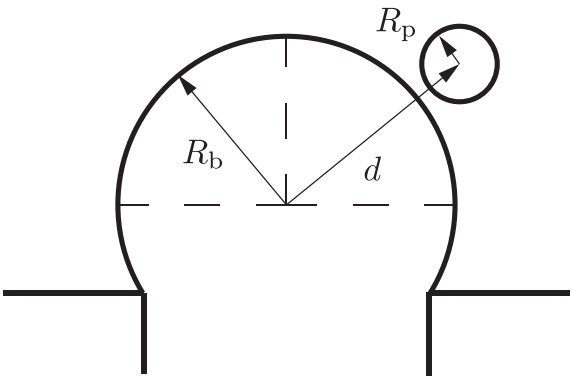

Figure 2.5: R_{b} and R_{p} are the radii of the bubble and particle, respectively. d is the center-to-center distance between the particle and bubble.

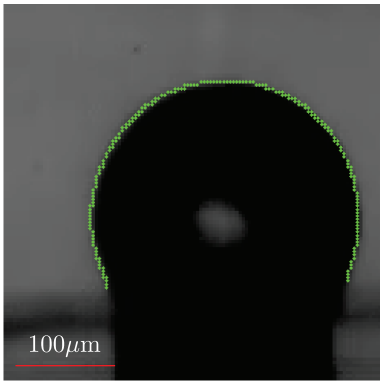

Figure 2.6: The edge of the bubble is detected by MATLAB.

we observe particles that have been stabilized onto the bubble surface at a high voltage being released into the external flow as the voltage is decreased. The critical voltage, V_{c}, at which the particles are released is recorded for a given frequency, f. In the second set (Exp B), we measure the critical voltage, V_{c}, at which an acoustic bubble is able to trap particles originally in motion for varying f. We define R_{b} and R_{p} to be the radii of the bubble and particle (see Fig. 2.5), respectively. d is the center-to-center distance between the particle and bubble . The experiments are recorded with a high-speed camera (Phantom Miro M310, Vision Research) from the side of the microchannel. For each experiment at

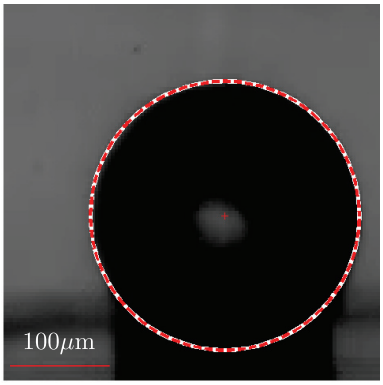

Figure 2.7: The edge of the bubble is fitted by least square error method to find a circle.

given V and f, the interaction between the bubble and particle is captured at 1000 fps (240 $\times$ 320 pixels), while the bubble oscillations are recorded at 120171 fps (128 $\times$ 128 pixels) with resultant images shown in Fig. 2.6 and Fig. 2.7.

2.2.2 Data Analysis

To measure the bubble oscillation amplitude, we use a MATLAB Canny function to detect the edge of the oscillating bubble. The edge of the bubble is expressed in terms of the coordinate of the pixel points (Fig. 2.6). We develop MATLAB algorithm to process all the images automatically to collect the data of all the videos with various frequencies and voltages. Once the coordinate of the bubble edge of all the videos has been determined, the least square error method is used to find a circle that best fits the edge (Fig. 2.7). Figure. 2.8 shows one example of the oscillation displacement at 21 kHz and 190 V as a function of the frame number calculated using the instantaneous bubble radius, $R(t)$, minus the equilibrium bubble radius $R_{\mathrm{b}} = 152.5\mu$m over 100 frames. The bubble amplitude is subsequently calculated by averaging over local maxima of $|R(t) - R_{\mathrm{b}}|$. The consistency and periodicity of the displacement in Fig. 2.8 demonstrate the effectiveness of our data analysis method.

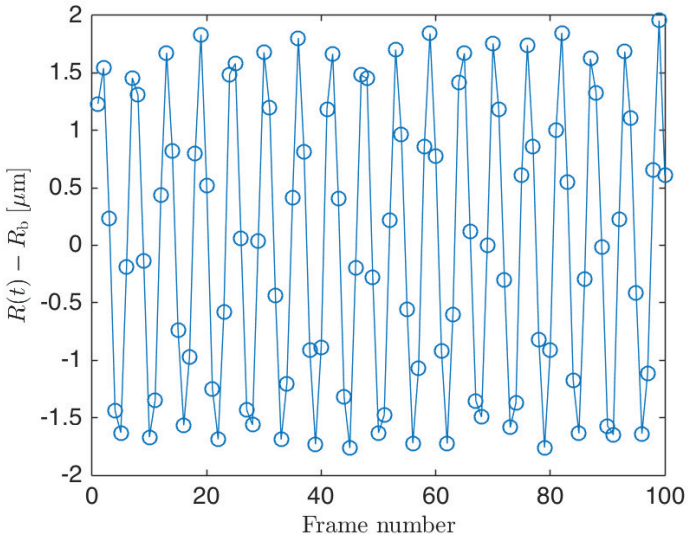

Figure 2.8: The plot shows the displacement of an oscillation bubble versus frame number at 21kHz and 190V calculated using fitted circle.

2.3 Results

2.3.1 Experimental Data

The dimensionless amplitude, ξ, of the bubble oscillation (scaled by the bubble radius, R_b) is extracted from single bubble oscillation videos of Exp B and is plotted as a function of f for given V in Fig. 2.9. The plot shows that the oscillation amplitude generally increases with V but varies nonlinearly with f. In particular, the acoustic bubble exhibits resonant behavior around $f = 21$ kHz and 35 kHz. In order to find the reason that causes the resonant behavior of the bubble, we also measure the amplitude of the whole device at 3 V. We find that the amplitude of the oscillation bubble as a function of the frequency matches the device resonance shown in Fig. 2.10, which indicates that the resonance behavior of the bubble is strongly affected by the whole device. The bubble resonant behavior appears to intensify with V at $f = 35$ kHz, as the bubble switches from volumetric to shape oscillations for V greater than 30 V (see Fig. 2.11). For a bubble un-

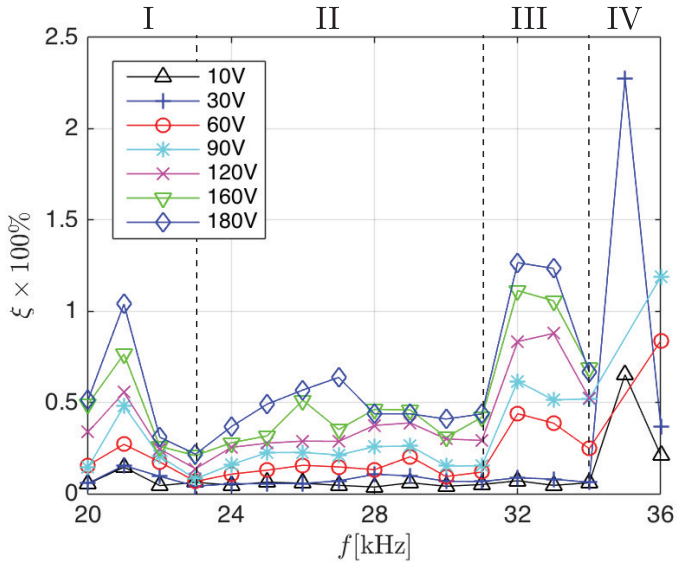

Figure 2.9: Dimensionless bubble amplitude, ξ, increases with V but varies nonlinearly with f.

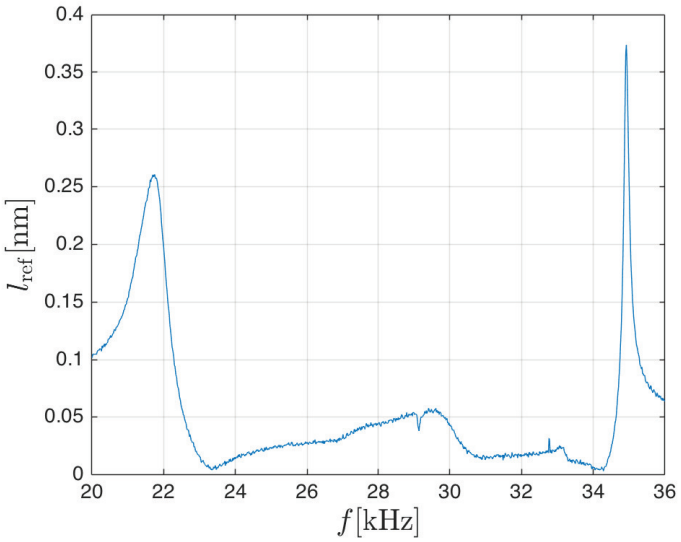

Figure 2.10: Device vibration amplitude l_{ref} exhibits resonant behavior at 21kHz and 35kHz for 3 V.

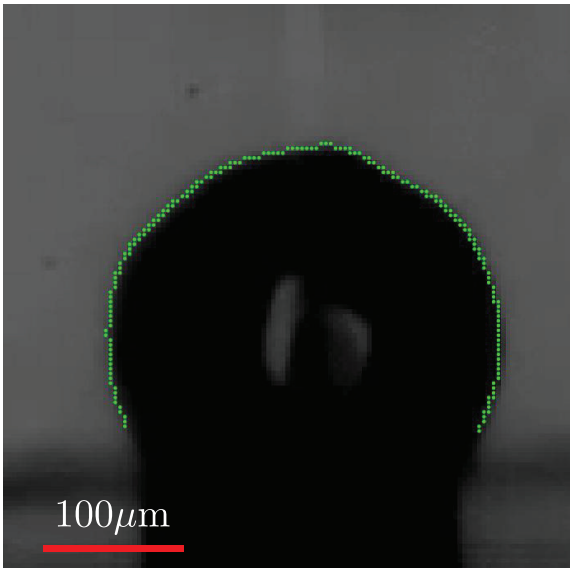

Figure 2.11: Snapshot of the oscillating bubble excited at 35kHz indicates that bubble switches from volumetric to shape oscillations for V greater than 30V.

der shape oscillation, the amplitude is no longer the same on the surface of the bubble at different direction. In this study, we will only focus on the effect of volumetric oscillations on particles and neglect the data range for V >30 V at 35 kHz.

The results of particle and bubble interaction data are summarized in a f-V phase diagram of Fig. 2.12: The triangular markers indicate the critical voltages for given f at which the particles are released from the bubble (Exp A), while the dots mark the frequencies and voltages at which the particles are trapped and remain on the bubble surface (Exp B). The phase diagram is overlaid with the gray scale map of ξ from Exp B, to show the correlation between the oscillation amplitudes and bubble's ability to trap particles. The dots overlap with the gray scale map, especially when the color of the map is geting darker. This indicates that the trapping of the particles is strongly related to the oscillation amplitude of the bubble. The critical bubble amplitudes, ξ_c, at the onset of particle releasing or trapping are plotted as a function of f in Fig. 2.13. Except for $f = 35$ kHz, most values of ξ_c fall in the

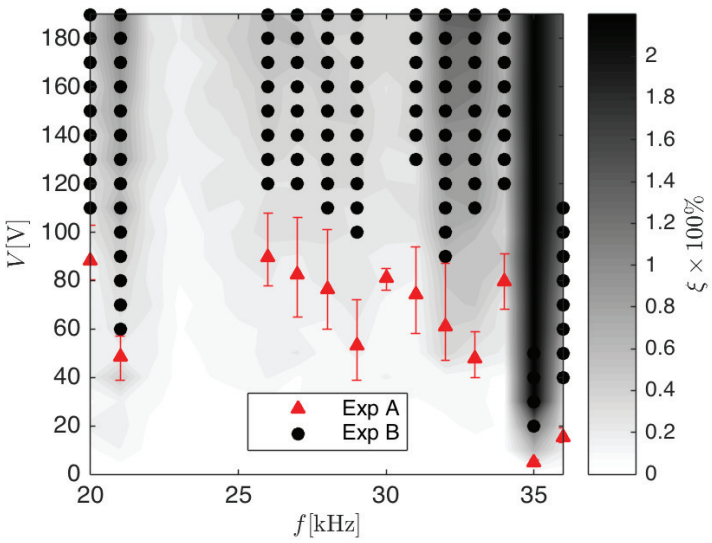

Figure 2.12: Phase diagram of experimental results from Exp A and Exp B.

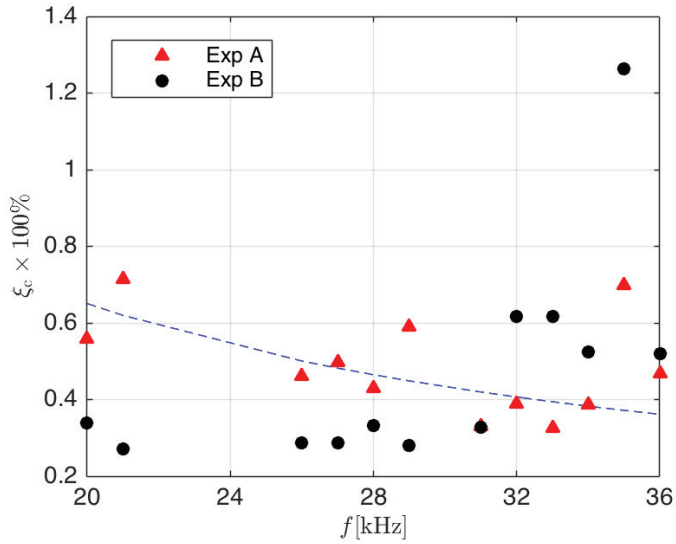

Figure 2.13: Critical oscillation amplitude, ξ_c, plotted as a function of f, with the emprical fit to Exp A as a dashed line.

range between 0.2%-0.8%.

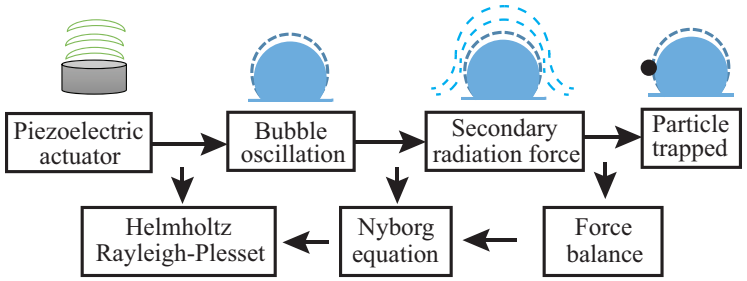

Figure 2.14: Flow chart of the working mechanism and corresponding theory for particle trapping. Upon the piezoelectric actuation, the bubble oscillates in response to acoustic pressure waves, and, in turn, generates a secondary radiation force, F_{SR}. The bottom row includes mathematical models that inform each physical process.

In order to derive the critical input voltage, V_{c}, that leads to particle trapping for given f, this work will use the following steps (see Fig. 2.14): first, perform force balance between the attractive secondary radiation force and the net hydrodynamic force on the particle to derive the critical bubble oscillation, ξ_{c}; second, linearize the Rayleigh-Plesset equation to solve for the critical pressure, p'_{c}, needed to generate ξ_{c}; finally, simplify the Helmholtz equation to relate p'_{c} to the critical applied voltage, V_{c}.

2.3.2 Critical Secondary Radiation Force

The secondary radiation force, F_{SR}, refers to the near-field attractive or repulsive force between the bubble and an object due to the pressure waves generated by the oscillating bubble [112]. The initial theoretical development of the secondary radiation force was made by Nyborg [14] who derived the following expression for F_{SR},

$$F_{\mathrm{SR}} = 4\pi\rho_{\mathrm{l}}\left(\frac{\rho_{\mathrm{p}}-\rho_{\mathrm{l}}}{\rho_{\mathrm{l}}+2\rho_{\mathrm{p}}}\right)\frac{R_{\mathrm{b}}^{6}R_{\mathrm{p}}^{3}}{d^{5}}\omega^{2}\xi^{2}, \tag{2.1}$$

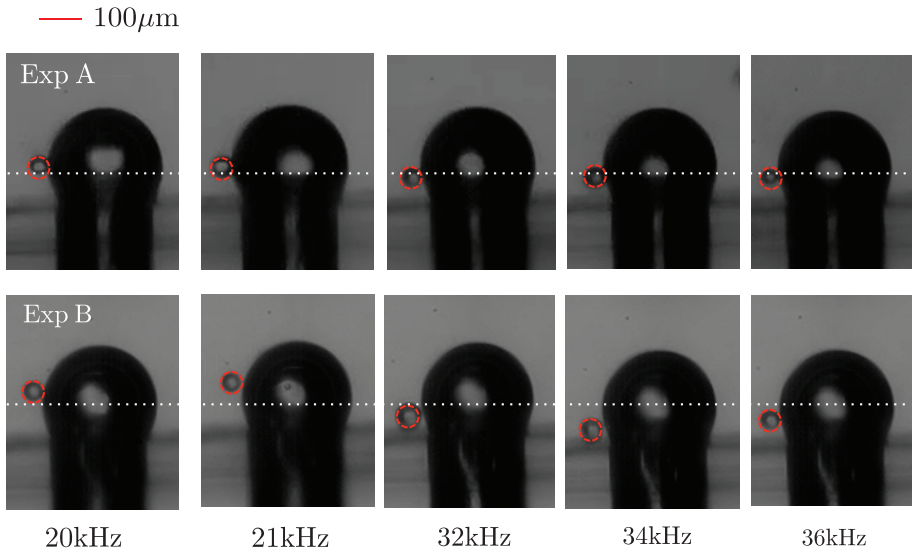

Figure 2.15: (a) Snapshots of particle locations at the onset of release (Exp A) and trapping (Exp B)

where ρ_{l} and ρ_{p} are the liquid and particle densities, respectively; R_{p} corresponds to the particle radius, and d is the center-to-center distance between the bubble and particle; $\omega = 2\pi f$ is the radian frequency.

Image sequences of the particle release and trapping locations in Exp A and Exp B are shown in Fig. 2.15. As shown in the images, the release location of the particle is observed to match the stagnation point of the bubble for all frequencies, ensuring that the net hydrodynamic force on the particle, F_{D}, must be constant for Exp A, while the particle trapping location in Exp B varies between experimental runs. Therefore, for the sake of simplicity, all the theoretical consideration from hereon will be limited to Exp A.

Based on a simple force balance depicted in Fig. 2.16, in the critical moment of particle release from the stagnation point, F_{D} must balance the threshold secondary radiation force, F_{SRc}, needed to hold the particle on the bubble (*i.e.*, if $F_{\mathrm{SR}} < F_{\mathrm{SRc}}$, the particle is released from the bubble). By plugging in the experimental values of ξ_{c} in Eq. (1), F_{SRc} is calculated and plotted in Fig. 2.17 to reveal that F_{SRc} is indeed constant for Exp A (trian-

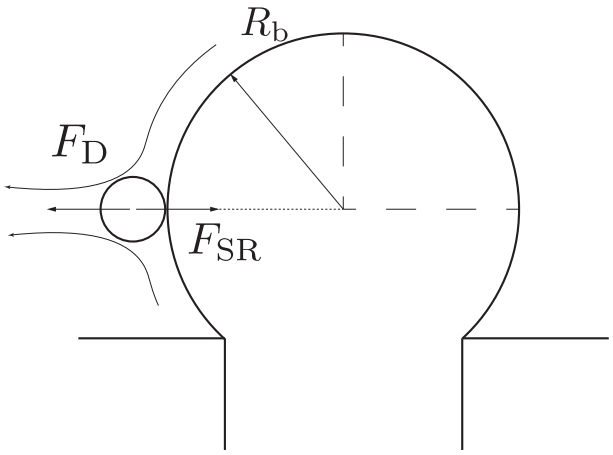

Figure 2.16: Schematic view of a particle located at the bubble stagnation point.

gle), as $F_{\mathrm{SRc}} = F_{\mathrm{D}} =$ constant. On the other hand, F_{D} can be estimated by considering a modified Stokes drag on a sphere (*i.e.*, micro-particle) experiencing a local straining flow near the stagnation point of another spherical obstacle (*i.e.*, bubble). Valid in the limit of $R_{\mathrm{p}}/R_{\mathrm{b}} \ll 1$, Goren and O'Neill[148] derived the expression for this modified drag as

$$F_{\mathrm{D}} = 6\pi f_0 \mu U_\infty \left(\frac{R_{\mathrm{p}}}{R_{\mathrm{b}}}\right)^2 R_{\mathrm{p}}, \tag{2.2}$$

where U_∞ is the external flow velocity at infinity, and μ is the liquid viscosity; f_0 is the correction factor that varies with the particle distance from the obstacle. While this expression has been derived for a solid obstacle that satisfies no slip boundary condition on the surface, it is reasonable to assume that the same functional relationship will hold for a bubble as an obstacle but with a different value of f_0.

Finally, by balancing F_{SRc} (Eq. (2.1)) with F_{D} (Eq. (2.2)), we can derive an expression for ξ_{c} upon particle release,

$$\xi_{\mathrm{c}} = \sqrt{\frac{3\mu U_\infty f_0(\rho_{\mathrm{l}} + 2\rho_{\mathrm{p}})d^5}{2R_{\mathrm{b}}^8 \rho_{\mathrm{l}}(\rho_{\mathrm{p}} - \rho_{\mathrm{l}})\omega^2}}, \tag{2.3}$$

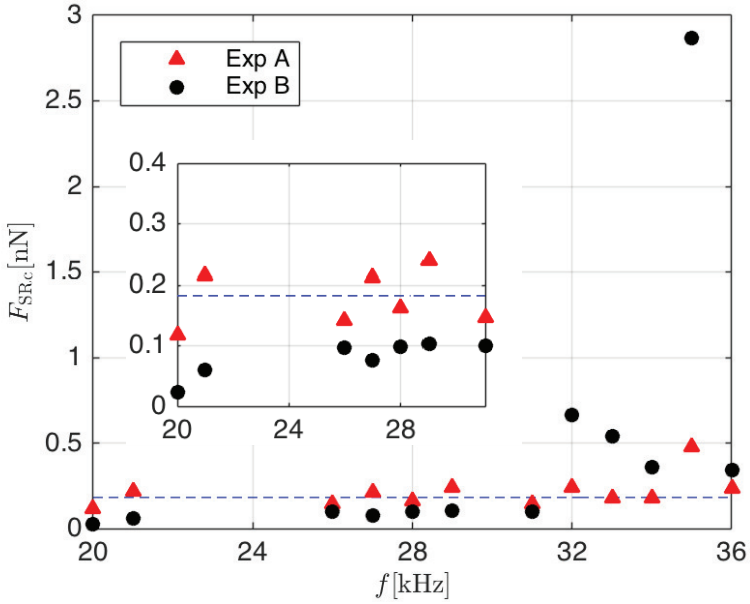

Figure 2.17: Critical secondary radiation force, F_{SRc} plotted as a function of f. The zoom-in plot shows the values from 20kHz to 30kHz.

where the value of correction factor, f_0, is found by empirically fitting Eq. (2.3) to data in Fig. 2.13. This allows us to quantify how the threshold bubble oscillation must depend on different physical parameters of the system, in particular, the driving frequency, f.

2.3.3 Threshold Acoustic Parameter

For isotropic, volumetric bubble oscillations, the relationship between the resultant oscillation amplitude and driving pressure is given by the Rayleigh-Plesset equation[149, 150],

$$R\ddot{R} + \frac{3}{2}\left(\dot{R}\right)^2 = \frac{1}{\rho_{\mathrm{l}}}\left(p_{\mathrm{g}} - p - 4\mu\frac{\dot{R}}{R} - \frac{2\sigma}{R}\right) \tag{2.4}$$

where R is the instantaneous bubble radius as a function of time and the overhead dot refers to differentiation with respect to time. Here, p_{g} and p correspond to the internal and external driving pressures of the bubble, respectively, while σ is the surface tension of the water/air interface. Since the bubble oscillation amplitude in our experiments is less

than 1%, we may linearize the Rayleigh-Plesset equation by assuming $R = R_0 + R'$ and $p = p_0 + p'$, where R' and p' are the small perturbations of the bubble radius and driving pressure (*i.e.*, $R'/R_0 \ll 1$ and $p'/p_0 \ll 1$). The solution to the linearized Rayleigh-Plesset equation yields a linear relationship between p' and R':

$$p' = R'/G, \tag{2.5}$$

where

$$G = \frac{R_\mathrm{b}^2}{\sigma}\left[\frac{Re_\mathrm{b}}{Ca_\mathrm{b}}\right]^2 \left\{ \frac{We_\mathrm{b} - H}{16(4 - \frac{Re_\mathrm{b}}{Ca_\mathrm{b}}H) - \left[\frac{Re_\mathrm{b}}{Ca_\mathrm{b}}(H - We_\mathrm{b}) - 8\right]^2} \right\}, \tag{2.6}$$

and

$$H = \frac{3\gamma p_0 R_\mathrm{b}}{\sigma} - 2 + 6\gamma, \tag{2.7}$$

with $\gamma = 1.4$ as the gas constant. Here we define Reynolds number, $Re_\mathrm{b} = \rho_\mathrm{l} R_\mathrm{b}(R_\mathrm{b}\omega)/\mu$, capillary number, $Ca_\mathrm{b} = \mu(R_\mathrm{b}\omega)/\sigma$, and Weber number, $We_\mathrm{b} = \rho_\mathrm{l}(\omega R_\mathrm{b})^2 R_\mathrm{b}/\sigma$, specific to the acoustic bubble, respectively. Since $R'_\mathrm{c} = \xi_\mathrm{c} R_\mathrm{b}$, Eq. (2.5) allows us to solve for the critical driving pressure, $p'_\mathrm{c} = R'_\mathrm{c}/G$.

The pressure field generated by the acoustic actuation of the device can be solved based on the Helmholtz equation,[151],

$$\nabla^2 p' + k^2 p' = 0, \tag{2.8}$$

where the wave number k is given by $k \sim \omega/c_\mathrm{a}$, and c_a is the speed of sound in water. In order to find the expression for the pressure inside the micro-channel in terms of the channel vibrating amplitude, we use a simplified one-dimensional model to simulate our experiment as shown in Fig. 2.18. The micro-channel vibrates in x-direction, and we let $2h$ be the height of the channel. In the case of one-dimensional propagation of pressure

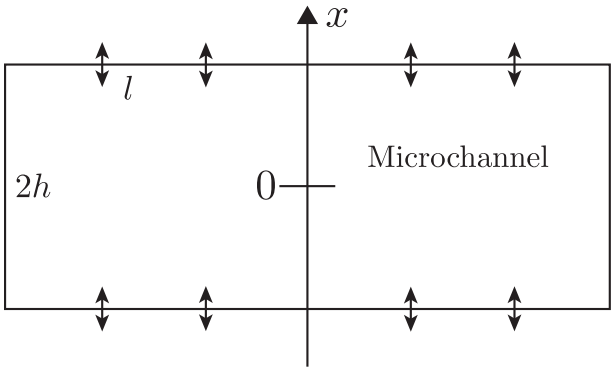

Figure 2.18: A schematic of one-dimensional model for the micro-channel. The channel is vibrating in x-direction, and L is the height of the channel.

waves, the solution to the Helmholtz equation is given by

$$p' = i{c_\mathrm{a}}^2 \rho_\mathrm{l} k l \frac{\sin(kx)}{\cos(kh)} e^{-i\omega t}, \tag{2.9}$$

where l is the device vibration amplitude. For simplicity, the device amplitude is assumed to increase linearly with V, or $l = K l_\mathrm{ref} V / V_\mathrm{ref}$, where l_ref is the reference device amplitude at 3 V shown in Fig. 2.10, and K is the fitting parameter whose value depends on the voltage regime. Since $kx \ll 1$ and $kh \ll 1$, we use the Taylor expansion to further simplify p' to

$$p' = K 4\pi^2 \rho_\mathrm{l} f^2 h l_\mathrm{ref} \left(\frac{V}{V_\mathrm{ref}} \right), \tag{2.10}$$

where h is the channel half-height.

Finally, combining Eq. (2.3), (2.5), (2.10) leads to the expression for the critical voltage that leads to particle release at given frequency:

$$\frac{V_\mathrm{c}}{V_\mathrm{ref}} = \frac{1}{J(f)} \frac{\sqrt{6}}{4\pi} \sqrt{f_0} U_\infty \sqrt{\frac{1}{Re_\mathrm{h}}} \sqrt{\frac{2\rho_\mathrm{p} + \rho_\mathrm{l}}{\rho_\mathrm{p} - \rho_\mathrm{l}}} \left[\frac{R_\mathrm{p}}{R_\mathrm{b}} + 1 \right]^{\frac{5}{2}} \sqrt{\frac{R_\mathrm{b}}{h}}, \tag{2.11}$$

where

$$J(f) = KGl_{\mathrm{ref}}We_{\mathrm{b}}f. \tag{2.12}$$

Each term in $J(f)$ is a function of the excitation frequency, f; here we define alternate Reynolds number with respect to the micro-channel as $Re_{\mathrm{h}} = \rho_{\mathrm{l}}U_{\infty}h/\mu$. This theoretical function of critical voltage must depend on the experimental parameters (*i.e.*, the particle and bubble radii). For instance, V_{c} is shown to decrease with increasing channel height, h. The quantification of V_{c} for particle release and trapping via an acoustic bubble will allow for the optimization of lab on a chip operating conditions to trap or sort micro-sized objects.

The value of the fitting parameter, K, that relates the device amplitude to the bubble amplitude, or the driving pressure, can be extracted by calculating the pressure, p', based on Eq. (2.5) for varying V. The corresponding dimensionless plot is shown in Fig. 2.19, which clearly exhibits four different voltage regimes for varying f. In regimes I, II, and IV, the pressure increases in an approximately linear fashion with the voltage at different rates, or K, while the pressure varies nonlinearly with the voltage in regime III. By plugging in the empirical values of K into Eq.(2.11), we plot the critical voltage V_{c} for varying f (dashed line) on the experimental phase diagram in Fig. 2.20, in particularly good agreement with Exp A. Notably, our current theoretical result can be easily extended to other acoustic devices by simply updating the reference device vibration amplitude l_{ref} and K in Eq. (2.12) to match the particular experimental setup.

2.4 Conclusions

In summary, we have hereby quantified the secondary radiation force, F_{SR}, of an acoustic bubble used to trap micro-objects in lab on a chip systems, by combining experiments and reduced modeling. Experimentally, we measure the minimum input voltage at given f needed for a single acoustic bubble to generate sufficient F_{SR} to trap and stabilize a

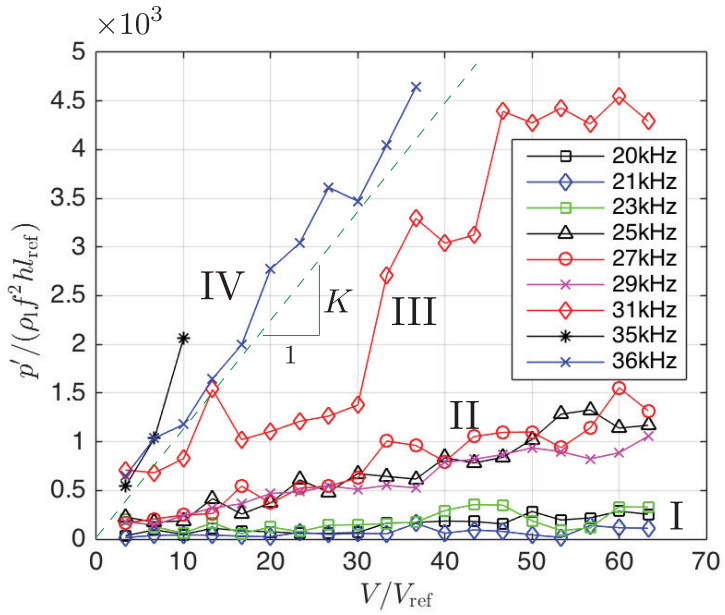

Figure 2.19: Dimensionless pressure, $p'/(\rho_l f^2 h l_{ref})$, increases in an approximately linear fashion in regime I, II and IV as a function of voltage V/V_{ref}, while it increases nonlinearly in regime III.

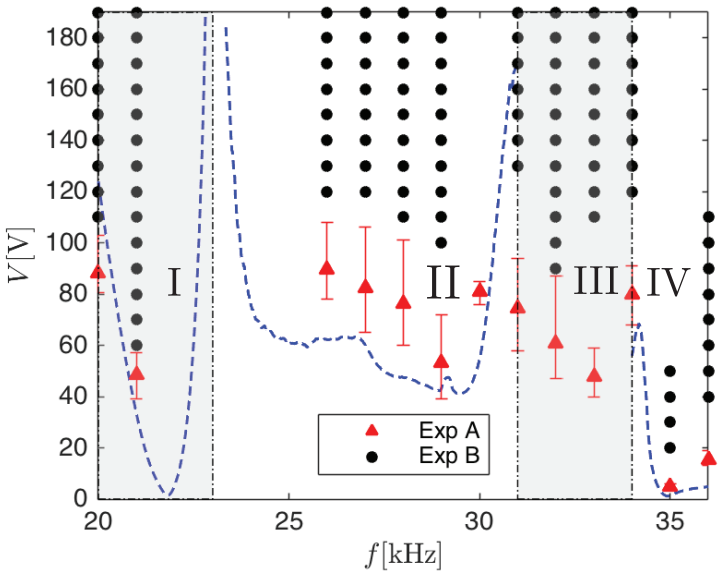

Figure 2.20: The dashed curve corresponds to the theoretical result, V_c ,based on the empirical values of K.

microsphere entrained in flow. This critical voltage is experimentally tested in two ways: by recording the maximum voltage at which an already attached particle is released from the bubble (Exp A) and the minimum voltage at which a particle entrained in flow is first trapped by the oscillating bubble (Exp B), as summarized in a phase diagram. For all experiments, the flow rate of water containing particle suspensions is kept constant and sufficiently high so that the effects of microstreaming flows can be neglected in our current study. In addition to measuring the onset behavior, the amplitude of bubble oscillation is also measured at the corresponding voltages and frequencies to verify the relationship between the oscillation amplitude and F_{SR}, as given by Nyborg [14].

In parallel to experiments, we combine well-developed theories to derive an expression for the critical input voltage that leads to the particle release into the external flow. By balancing the hydrodynamic force on a sphere near a stagnation point [148] with F_{SR}, a functional relationship between the threshold bubble oscillation and experimental parameters, such as particle size and driving frequency, is derived. Then, linearized Rayleigh-Plesset and Helmholtz equations are employed to connect this threshold bubble amplitude to the driving pressure, then to the applied voltage. Aided by empirical parameters to determine the vibration amplitude of the channel, the resultant expression for the critical voltage, V_{c}, is an explicit function of the driving frequency, f, and is in good quantitative agreement with the data from Exp A. While the final result, $V_{\mathrm{c}}(f)$, has been tested for our particular experimental setup, its theoretical approach and result should be valid for a wide range of acoustic devices and can easily accommodate them by adjusting the device vibration amplitude.

Overall, our work here takes an initial step to quantitatively analyze the secondary radiation force of an acoustic bubble for particle trapping and release in a flow. Therefore, this work paves the way towards future design of next-generation acoustic-based lab on a chip devices for more versatile applications. Future work includes developing a better

mathematical model for the hydrodynamic forces on the particle near the oscillating bubble surface. On the experimental side, performing the analogous experiments with a wide range of particle and bubble sizes and measuring the pressure field based on PIV (Particle Image Velocimetry)[152] will help validate our current model. Furthermore, extending this work to include multiple bubbles, microstreaming effects, or non-spherical objects is also of great practical interest for lab on a chip applications.

3. VISCOUS FINGERING OF A DRAINING SUSPENSION

3.1 Introduction

Viscous fingering at fluid-fluid interfaces is ubiquitous in all processes that involve more than one fluid [46, 153, 154, 155] and has direct implications in oil recovery. For instance, when water and polymers are injected into oil reservoirs to stimulate production - known as polymer flooding [156], viscous fingering is known to reduce sweep efficiency and lead to an early breakthrough of the injected fluid. In hydraulic fracturing that extracts natural gases and oil from impermeable reservoirs [157, 158], viscous fingering enables the deeper penetration of the fracturing fluid into fractures and results in the enhanced transport of sand-like particles, or proppant [159, 160]. Therefore, fundamental understanding of viscous fingering may lead to the control of various oil recovery processes.

A flow configuration that is particularly relevant for oil and hydrocarbon recovery is the fluid drainage from a large reservoir into a smaller region (*i.e.* well). Motivated by this physical picture, Paterson [44] experimentally observed that when the oil withdraws from air in a radial sink flow, the oil-air interface becomes unstable, and the oil drainage stops once the fastest growing finger reaches the well. The analogous fingering behavior was also investigated theoretically by calculating the interfacial shapes of a 2D circular drop subject to suction [64, 161]. More recently, Chen and colleagues [51, 54, 52] numerically investigated the nonlinear interfacial patterns in the suction-driven Hele-Shaw problem, based on a diffuse interface method. Compared to extensive works on viscous fingering both in rectilinear and radial source flows [46, 153, 154, 44, 155], the study of "inward" viscous fingering remains limited even for pure liquids and non-existent for more complex fluids, such as suspensions. Suspensions are particularly commonplace in oil recovery applications that include hydrocarbon recovery through proppant packs [162, 163].

Interestingly, the interfacial dynamics of suspensions deviate from their pure liquid counterparts in diverse flow types. For instance, the addition of particles to the fluid accelerates the onset of the droplet pinch-off, as the thread thins down to a particle length-scale [164, 165, 166, 167, 168, 169]. Excess particles can also suppress viscous fingering in particle-laden flows down an incline [170, 171, 172, 173, 174, 175, 176, 177, 178], while the injection of a suspension into a Hele-Shaw cell leads to fingering due to the particle accumulation on the fluid-fluid interface [179, 180, 181, 182]. In addition, various interfacial patterns are observed when air is injected into a fluid-particle mixture [183, 184, 185, 186, 187]; specifically, Sandnes and co-authors [186] observed complex transitions in suspension-air morphologies (*i.e.,* from solid-like, "frictional" to liquid-like, "viscous" regimes) with an increasing injection rate of air.

Given the prevalence of particles in oil recovery processes and their significance in interfacial dynamics, we will presently build on the work of Paterson [44] and consider the viscous fingering of a draining suspension. Specifically, we experimentally test the effects of neutrally buoyant particles on the dynamics of the fastest growing finger that directly controls the total oil recovered, as suspensions withdraw into a well from a Hele-Shaw cell. The experimental results in Sec. 3.3 reveal that the finger grows faster with particle concentrations, ϕ_0, while the total drainage time and the amount of recovered oil also increase with ϕ_0. These contradictory results allude to the dual effects of suspended particles to delay and to accelerate fingering. In addition, particles of select sizes are observed to coat the channel surfaces and do not drain, reminiscent of colloidal assembly in dip coating [188].

Following the experimental setup and data analysis in Section 3.2, experimental results are reported in Section 3.3, consisting of the finger growth speed in Section 3.3.1 and total time of drainage in Sections 3.3.2. Section 3.3.3 studies the experimental results and simplified models of particle drainage versus entrainment. The summary and future

directions are given in Section 3.4.

3.2 Methods

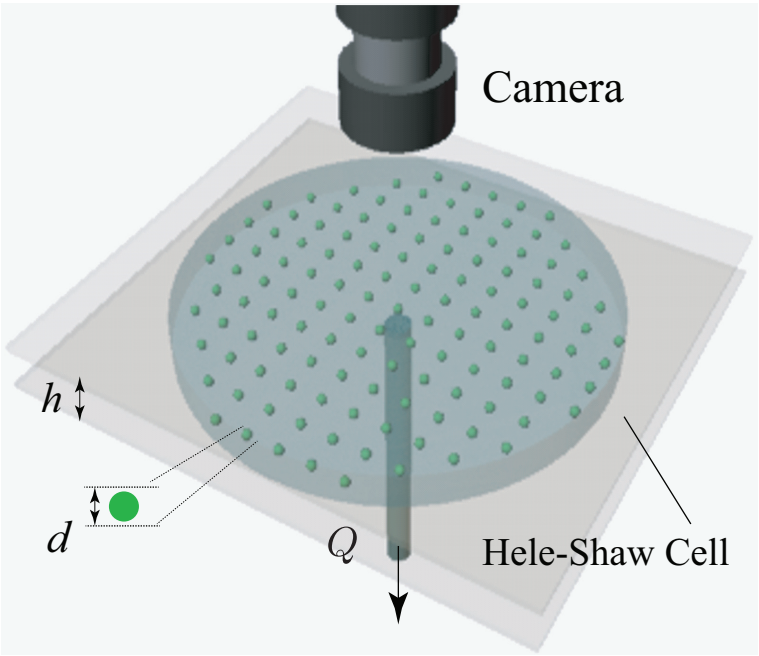

Figure 3.1: Schematic of the experimental setup.

3.2.1 Experimental Setup

We conduct the suspension drainage experiments in a Hele-Shaw cell that consists of two parallel plexiglass plates $(30.5 \times 30.5 \times 3.8\,\mathrm{cm})$. The plates are separated by a gap thickness $h = 1.39\,\mathrm{mm}$; the bottom plate has a small hole drilled in the center through which the suspension is drained (Fig. 3.1). The suspension of the particle volume fraction, ϕ_0, is prepared by mixing neutrally buoyant polyethylene particles (density $\rho_\mathrm{p} = 1.00\,\mathrm{g/cm^3}$, diameter $d = 130\,\mu\mathrm{m}$; Cospheric) with a PMMS silicone oil (density $\rho_\mathrm{l} = 0.96\,\mathrm{g/cm^3}$ and dynamic viscosity $\eta_\mathrm{l} = 0.096\,\mathrm{Pa\cdot s}$) in a syringe. The value of ϕ_0 is varied

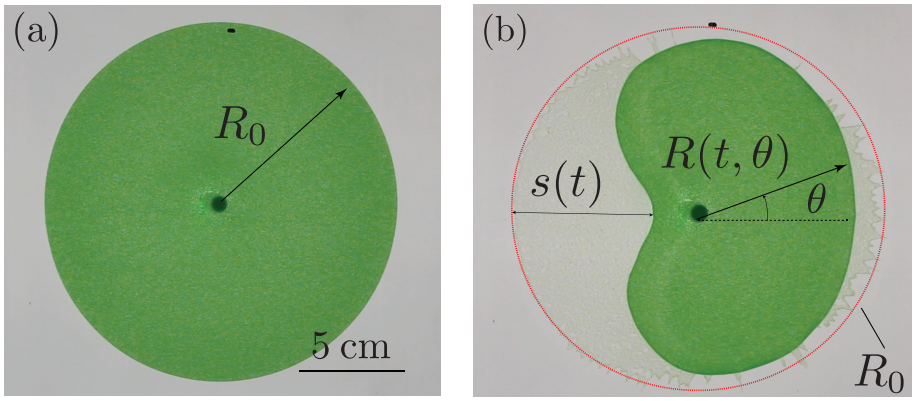

Figure 3.2: (a) Initial circular shape of the suspension with $\phi_0 = 0.1$ and radius $R_0 \approx 10\text{cm}$. (b) $R(t,\theta)$ is defined as the distance from the center to each point of the interface at given time, t, while $s(t) = |R_0 - R_{\min}(t)|$.

between 0.05 and 0.2 with an increment of 0.01.

We first inject the suspension into the Hele-Shaw cell to the radius of $R_0 \approx 10\,\text{cm}$ (Fig. 3.2(a)). Notably, the maximum value of ϕ_0 is set at 0.2 to prevent the inhomogeneous distribution of particles and miscible fingering upon initial injection, as previously observed by Xu and colleagues [181]. The suspension is then withdrawn from the center at a fixed flow rate, Q (*i.e.,* $Q = 5,\ 6,\ 6.5,\ 7.5$ and $10\,\text{ml/min}$). A high resolution camera (1920×1080 pixel images, FOV $60°$) records the suspension drainage experiments from directly above the Hele-Shaw cell. The instantaneous radius $R(t,\theta)$ corresponds to the distance from the center to each point on the interface at an angle, θ, and is obtained using MATLAB image processing tools. We also extract the instantaneous area of the draining suspension $A(t)$ and its time-rate of change $\dot{A}(t)$, based on $A(t) = (1/2)\int_0^{2\pi} R^2(t,\theta)d\theta$ (Fig. 3.2(b)). In particular, we focus on the average value of $\dot{A}(t)$ over the total drainage time, t_c.

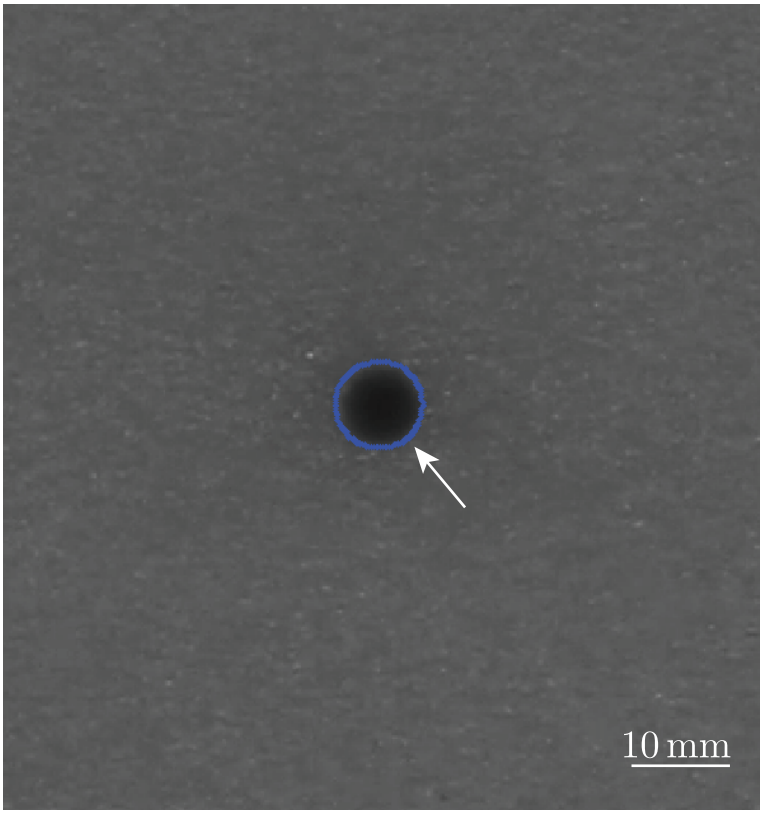

Figure 3.3: The edge of the center hole is first detected and diameter is measured.

3.2.2 Image Processing and Data Analysis

The total number of the images extracted from each video is over 1000. In order to reduce the processing time of each video, we take out 1 frame for every 50 frames and assign those frames with new numbers starting from 1. Since the camera has a 30 FPS (1/30 sec between each frame), therefore the time between each frame after re-ordering is 5/3 sec, which is used to calculate the time between any frames.

We use Canny function in MATLAB to detect the edge in the images. The Canny function detects the edge according to the pixel gradient, and the detected edges are represented in terms of pixel points. Before we start detecting the edge of the interface, we first measure the diameter of the center hole in the first frame in terms of number of pixels

(Fig. 3.3). Since we know the actual diameter of the hole from the experimental setup, which is 3.955 mm, we can calculate the ratio between the number of pixels to millimeter. This ratio is used to translate the measured number of pixels into actual distance from the images. We then process the all the images automatically to detect the edges of the interface for every videos. Examples of detected edges for two different frames are shown in Fig. 3.4 and Fig. 3.5. Initially, the shape of the suspension is close to a circle, therefore we can use best fit circle to find the initial radius of the suspension, R_0 in the first frame. Once the finger occurs as shown in Fig. 3.5, the distance between the finger tip is shortest among all the points on the edge. Hence the finger tip is then found by taking the minimum value of the distance from the edge to the center. We then calculate the deviation $s(t)$ as the absolute difference between R_0 and the finger tip. Once we collect all the values of deviation s for each experiment and plot it as a function of time, we use curve fitting in MATLAB using the exponential function to find the growth rate b. Finally, we can use the integration function to calculate the whole area of the suspension enclosed by the detected edge for each frame, $A(t)$.

In order to show the uncertainty of the measured values from the experimental setup, we add error bars to each of our figures. The errors are calculated according to [189]

$$\Delta y = \sqrt{\left(\frac{\partial y}{\partial G_1}\Delta G_1\right)^2 + \left(\frac{\partial y}{\partial G_2}\Delta G_2\right)^2 + \cdots + \left(\frac{\partial y}{\partial G_{\mathrm{N}}}\Delta G_{\mathrm{N}}\right)^2} \tag{3.1}$$

where $y = y\left(G_1, G_2, \ldots, G_{\mathrm{N}}\right)$. Here y is the value we would like to calculate and show in the plot, and $G_1, G_2, \ldots, G_{\mathrm{N}}$ are the data directly collected from the experiments. ΔG is the error from the experimental setup. For instance, there are errors from the pump flow rate, shim thickness and image processing, which all needs to be considered when calculating the error, Δy.

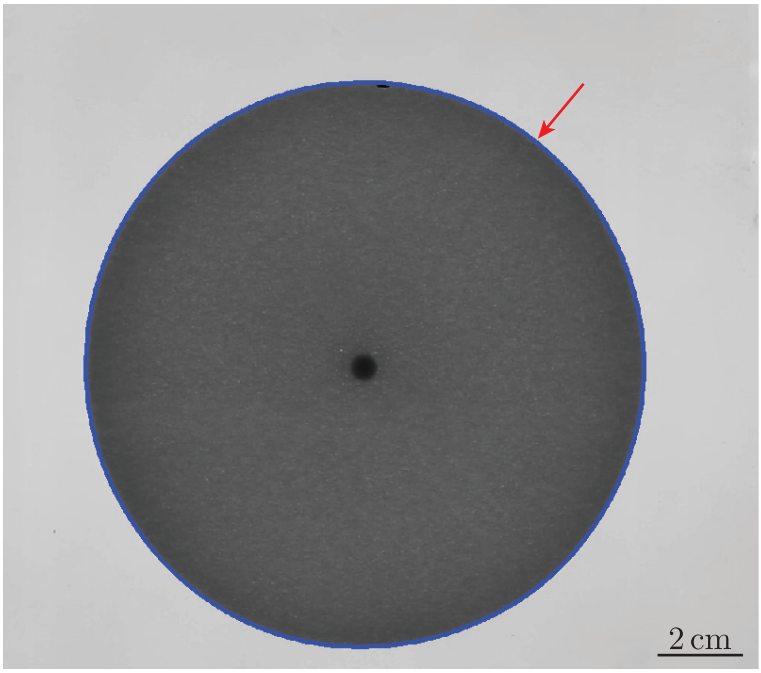

Figure 3.4: An example of detected edge for frame #5 at $\phi_0 = 0.2$, $Q = 5\,\mathrm{ml/min}$.

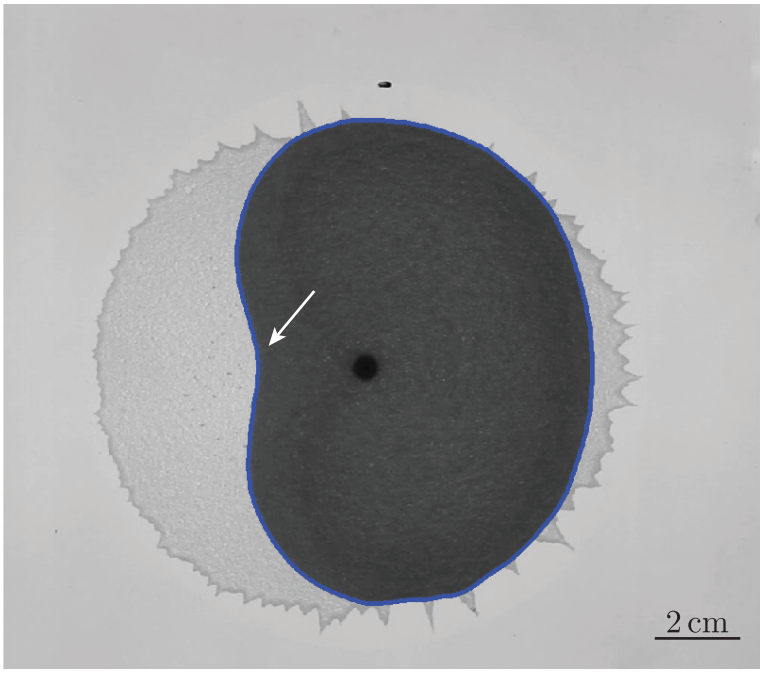

Figure 3.5: An example of detected edge for frame #150 at $\phi_0 = 0.2$, $Q = 5\,\mathrm{ml/min}$.

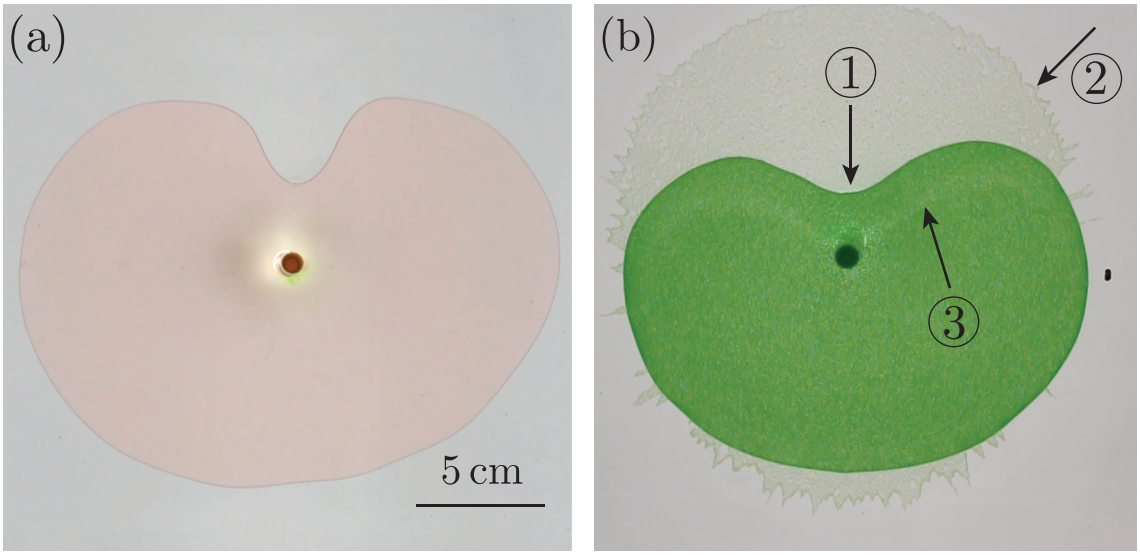

Figure 3.6: (a) An example of viscous fingering in a pure oil with viscosity $\eta_l = 0.096\,\mathrm{Pa{\cdot}s}$ at $Q = 10\,\mathrm{ml/min}$. (b) An example of viscous fingering in a suspension with $\phi_0 = 20$ and $Q = 7.5\,\mathrm{ml/min}$. Various phenomena are observed during the drainage.

3.3 Results

Before we add particles into the oil, we first perform the experiment with pure oil at $Q = 10\,\mathrm{ml/min}$ as a reference result (Fig. 3.6 (a)). Once the draining starts, the initial circular shape of the oil shrinks isotropically. At a certain time, one side of the edge becomes flat followed by the onset of fingering. Eventually, the draining stops once the finger reaches the center of the Hele-Shaw cell. The shape of the oil during drainage from our experiment qualitatively matches the numerical results from Kelly and Hinch [190]. Various physical phenomena emerge when a suspension as shown in Fig. 3.6 (b), instead of pure oil, drains from the air in a radial sink flow. First of all, we observe finger occurring at some time spot, similar to the pure oil case; then we find that some particles are left behind on the plates and provide pinning sites for the retracting air-suspension interface, leading to complex interfacial morphologies; thirdly, we also observe a different layer of suspension inside the bulk, which is the miscible fingering due to the inhomogeneous

distribution of the particle volume fraction. However, despite such added complexities, the most critical aspect of inward fingering experiments [44, 45] appears intact: the oil recovery stops when the dominant finger reaches the center hole, which will be the focus of our present work.

In particular, only one finger is observed after the drainage ceases in all our experiments. This is in contrast to what Paterson [44] and Thome et.al [45] had observed, in which there were multiple fingers. This is because the number of fingers increases at higher effective capillary number, $Ca = \eta_{\text{eff}} U/\gamma$ [52]. Here, $\eta_{\text{eff}} = \eta_{\text{l}}$ is the viscosity of the liquid for a pure fluid, while for a suspension η_{eff} is expressed as [191]

$$\eta_{\text{eff}} = \eta(\phi_0)/\eta_{\text{l}} = 1 + 2.5\phi_{\text{m}}^2(\phi_{\text{m}} - \phi_0)^{-1} + 0.1\phi_0^2\,(\phi_{\text{m}} - \phi_0)^{-2} \tag{3.2}$$

where $\phi_{\text{m}} \approx 0.62$ is the maximum packing fraction. η_{eff} is increasing when adding more particles into the oil as shown in Fig. 3.7. In our experimental setup, the effective viscosity of the suspension is typically around three times of the pure silicone oil. U and γ are the characteristic velocity of the interface and the surface tension coefficient. The highest capillary number in our experiment is $Ca \approx 3 \times 10^{-3}$, while for Paterson's experiment[44] $Ca \approx 5 \times 10^{-3}$, which is greater than ours. In the simulation work from Chen et.al[52], they use capillary $Ca > 10^{-1}$ and observe more vigorous fingers than in Paterson's experiment. The purpose of our current work is to focus on the growth speed of the dominant finger, therefore we keep our capillary number small so that only one finger occurs after the drainage stops.

In Fig. 3.8, the time-evolution images of the suspension of $\phi_0 = 0.1$ illustrate the typical suspension drainage experiment set at $Q = 7.5\,\text{ml/min}$. From the start of drainage (*i.e.* $t = 0\,\text{s}$), the suspension-air interface starts retracting towards the center; the interface moves non-axisymmetrically as the displacement of a viscous liquid by air is inherently

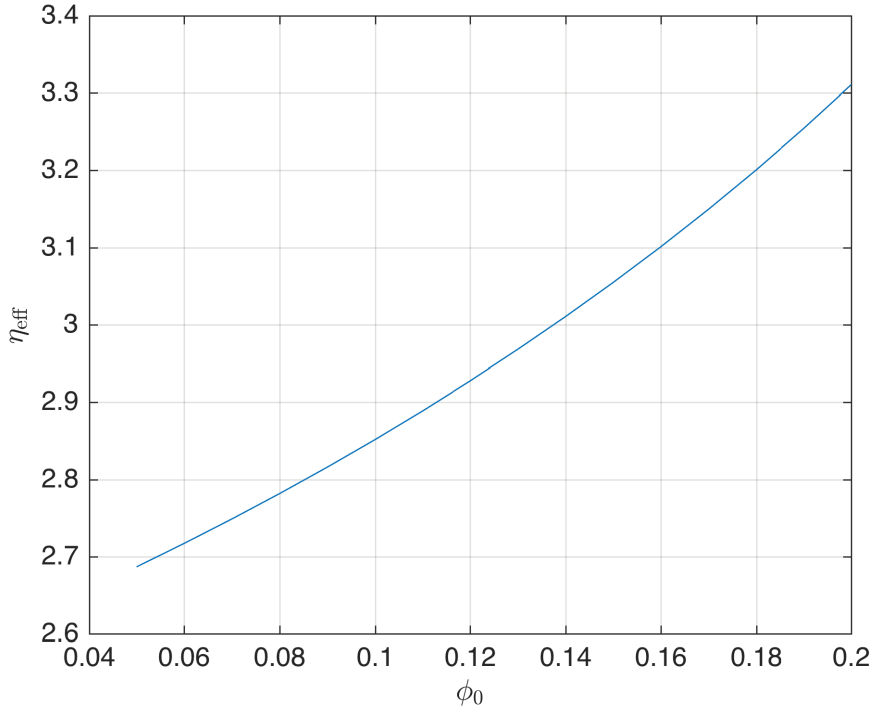

Figure 3.7: The effective viscosity, η_{eff}, is increasing with the particle volume fraction, ϕ_0

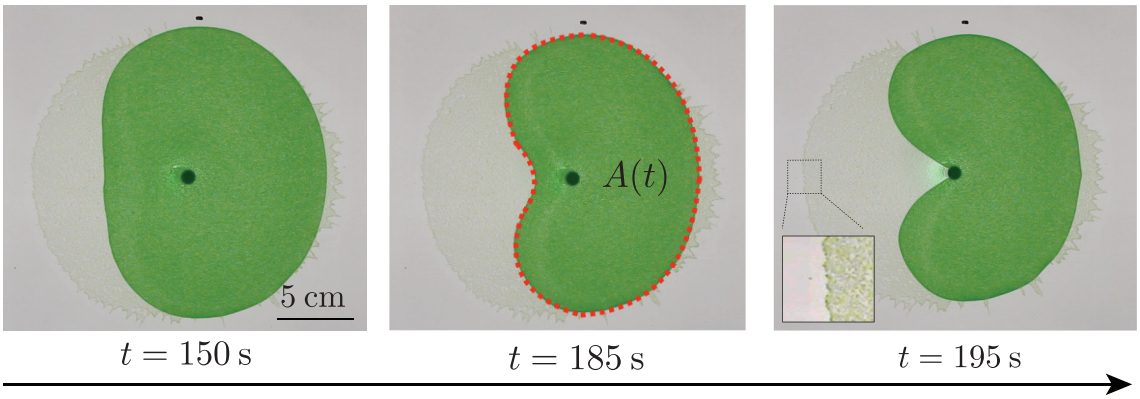

Figure 3.8: Time-evolution images of a $\phi_0 = 0.1$ suspension that is drained at $Q = 7.5\,\text{ml/min}$. A finger initiates after $t = 150\,\text{s}$ and grows until it reaches the center. $A(t)$ is defined as the instantaneous area of the draining suspension.

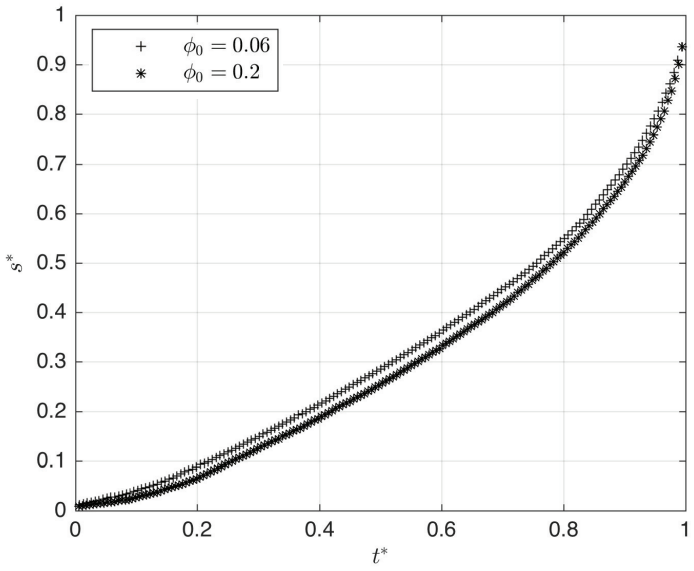

Figure 3.9: The plot of the time evolution of $s^* = s/R_0$ for varying ϕ_0 at $Q = 5\,\mathrm{ml/min}$.

unstable [46, 44, 155]. The interface becomes flat on one side at $t = 150\,\mathrm{s}$ and starts to finger inwardly. Accordingly, the onset of a viscous finger is defined as the moment of transition in interfacial shape from convex to concave at $t = 185\,\mathrm{s}$. We define the time it takes from $t = 0\,\mathrm{s}$ to the onset of finger as t_f. Upon its formation, the finger continues to grow towards the center, and the drainage ceases once the fingertip reaches the center at $t_\mathrm{c} = 195\,\mathrm{s}$. Hence, the dynamics of the finger must directly determine the total amount of recovered oil. In particular, after the drainage stops, we observe clearly a thin film of particles left on the surface as the zoom-in at $t = 195\,\mathrm{s}$ (Fig. 3.8).

3.3.1 Finger Growth Speed

The evolution of the growing finger is quantified by extracting the deviation of the minimum distance to the interface, $R_\mathrm{min}(t)$, from the initial radius, R_0, such that $s(t) = |R_0 - R_\mathrm{min}(t)|$. The dimensionless deviation, $s^* = s/R_0$, is plotted in Fig. 3.9 as a function of dimensionless time, $t^* = t/t_\mathrm{c}$, for $\phi_0 = 0.06$, 0.12 and 0.2, respectively, at

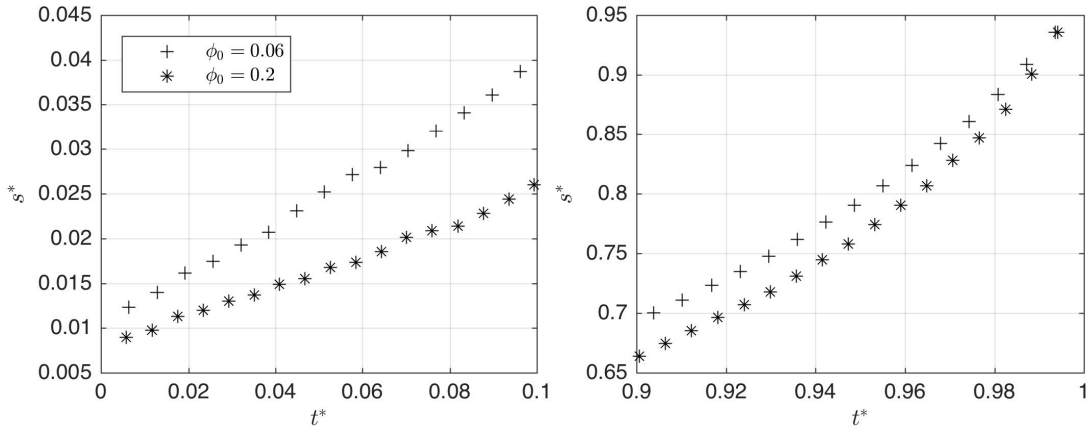

Figure 3.10: The plots show zoom-in of s^* for $t^* = 0 - 0.1$ and $t^* = 0.9 - 1$, respectively.

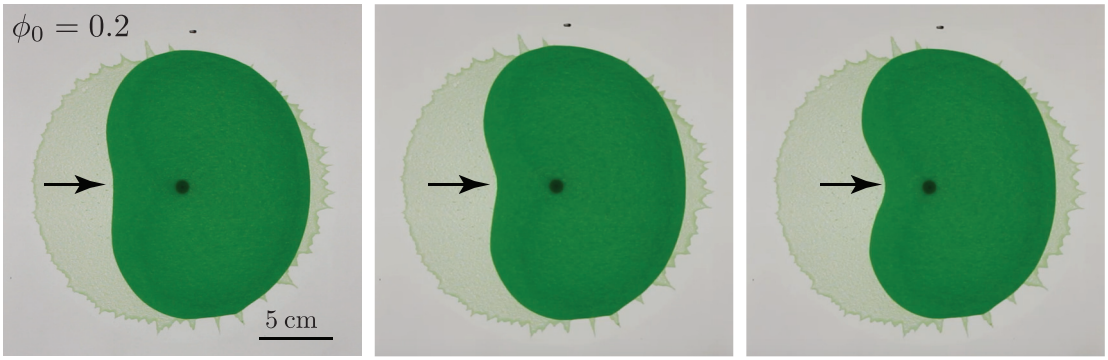

Figure 3.11: Time-evolution images of suspension from $t^* = 0.85 - 0.95$ at $\phi_0 = 0.2$ and $Q = 5\,\mathrm{ml/min}$ show that the fingering onset occurs at $t^* = 0.9$.

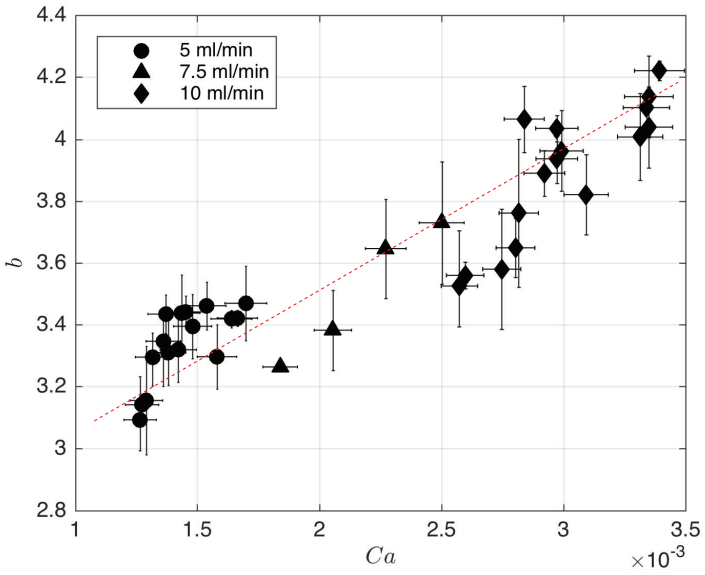

Figure 3.12: The dimensionless growth rate, b, is extracted by fitting the $s^* - t^*$ curve with the exponential function, $s^* \propto \exp(bt^*)$, for $t^* = 0.9 - 1$; the value of b is plotted as a function of the effective capillary number, Ca.

$Q = 5\,\mathrm{ml/min}$. The two plots in Fig. 3.10 of s^* versus t^* reveal different short-time and long-time behaviors for varying ϕ_0. Between $t^* = 0$ and 0.1, $s^*(t^*)$ increases more slowly for greater ϕ_0 (*i.e.* smaller $\dot{s}^*(t^*)$ for increasing ϕ_0), while the trend is reversed for $t^* = 0.9 - 1$. When we investigate the image sequences from $t^* = 0.85 - 0.95$ in Fig. 3.11, we find that this transition in $\dot{s}^*(t^*)$ at $t^* = 0.9$ corresponds to the initiation of a finger, as corroborated by the right figure in Fig. 3.10 for $\phi_0 = 0.2$. Hence, the slope of $s^*(t^*)$ for $t^* > 0.9$ must reflect the growth rate of the dominant finger that reaches the injection hole. Then, the dimensionless growth rate, b, is obtained by empirically fitting the experimental data to the exponential function, $s^* \propto \exp(bt^*)$, for $t^* > 0.9$.

At given Q, b clearly increases with ϕ_0, which can be rationalized by considering the effect of suspended particles on the overall viscosity, $\eta(\phi_0)$, as defined previously. An increase in ϕ_0 corresponds to a higher viscosity difference between the suspension and

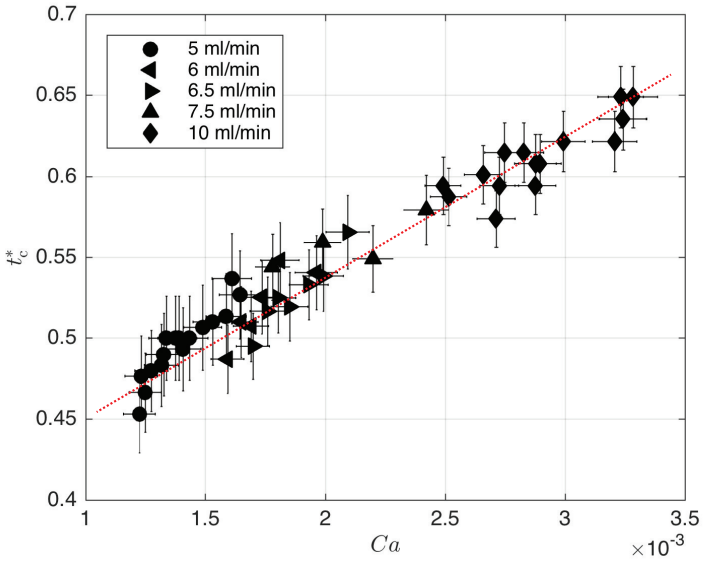

Figure 3.13: The dimensionless time of completion of drainage, $t_c^* = t_c|\dot{A}|/(\pi R_0^2)$, increases with the effective capillary number, Ca. Notably, t_c^* is analogous to the dimensionless volume of the drained suspension. The inset figure shows that dimensional t_c increases with ϕ_0 for $Q = 5\,\mathrm{ml/min}$.

air, or $\eta(\phi_0) - \eta_{\mathrm{air}}$, and must lead to a faster growing finger. For a wide range of ϕ_0 and Q values, b collapses onto a single curve as a function of the effective capillary number, $Ca = \eta(\phi_0)|\dot{A}|/(\gamma 2\pi R_0)$. Here, $|\dot{A}|/(2\pi R_0)$ represents the characteristic velocity of the retracting interface. The resultant plot in Fig. 3.12 shows the monotonic increase in b with Ca. This qualitatively agrees with the numerical simulations of Kelly and Hinch [190] who found the finger tip velocity to increase with the capillary number in the case of a draining liquid.

3.3.2 Total Time of Drainage Completion

From the oil recovery standpoint, the most important result to consider is the total time of drainage, t_c, which directly corresponds to the total volume of the recovered suspension, or $V_t = Qt_c$. Surprisingly, despite the increase in the fingertip speed, b, with

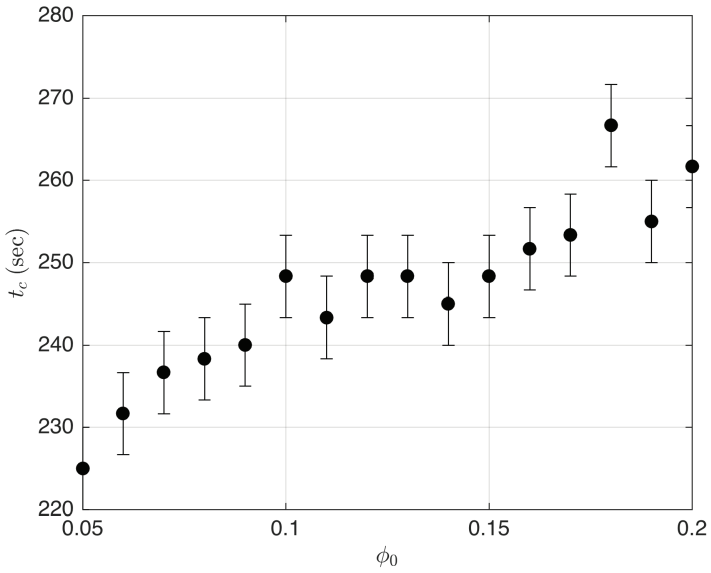

Figure 3.14: Dimensional $t_{\rm c}$ increases with ϕ_0 for $Q = 5\,{\rm ml/min}$.

Ca (see Fig. 3.12), the dimensionless completion time, $t_{\rm c}^* = t_{\rm c}|\dot{A}|/(\pi R_0^2)$, also increases with the effective capillary number in Fig. 3.13. Similarly, the value of dimensional $t_{\rm f}$ also increases with ϕ_0 as shown in Fig. 3.14. The counterintuitive correlation between the fingertip speed and the drainage time demonstrates that the onset of finger formation must be delayed with increasing ϕ_0. We extract the time of fingering onset, $t_{\rm f}$, from the experiments and plot it as a function of Ca in Fig. 3.15. Obviously, the dimensionless time of fingering onset, $t_{\rm f}^* = t_{\rm f}|\dot{A}|/(\pi R_0^2)$, increases with the effective capillary number. Similarly, the value of dimensional $t_{\rm f}$ also increases with ϕ_0 as shown in Fig. 3.16. This unexpected result suggests that the inclusion of particles may effectively increase the total drainage time and improve the production of oil.

The delay in the fingering onset cannot be explained by simply considering the effect of particles on the effective viscosity alone. In the pure liquid counterpart, fingering occurs sooner when the viscosity ratio between the invading and defending fluids is increased

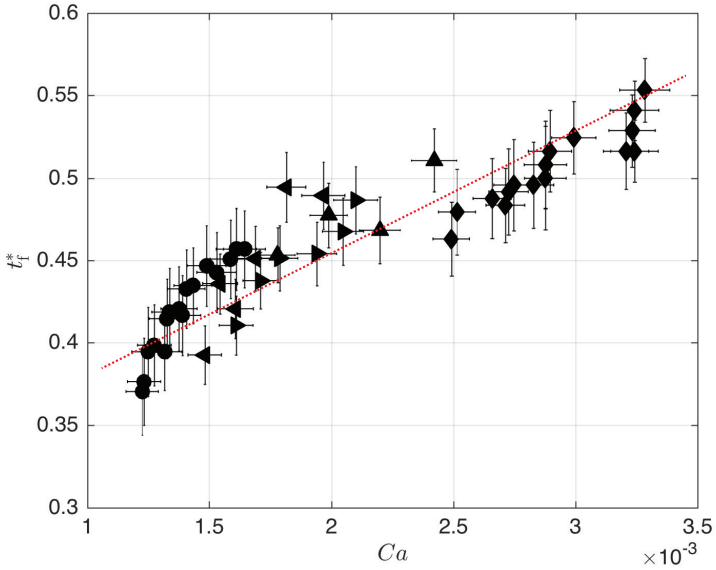

Figure 3.15: The dimensionless time of fingering onset, $t_{\mathrm{f}}^* = t_{\mathrm{f}}|\dot{A}|/(\pi R_0^2)$, increases with the effective capillary number, Ca.

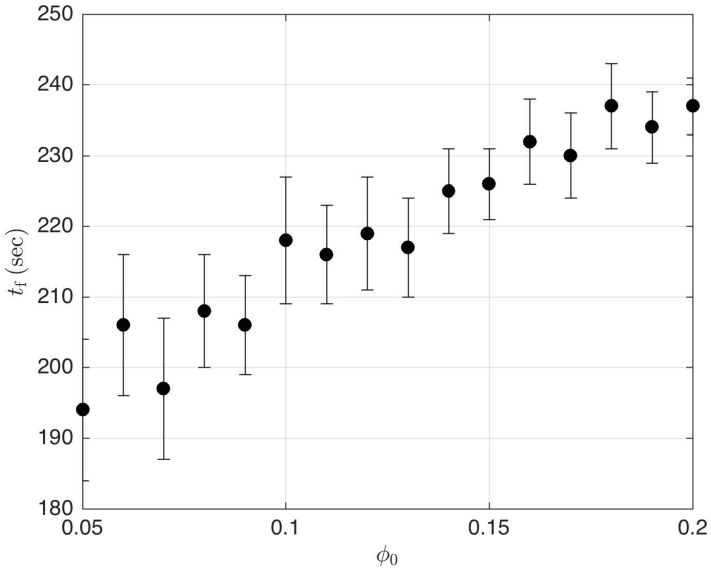

Figure 3.16: Dimensional t_{f} increases with ϕ_0 for $Q = 5\,\mathrm{ml/min}$.

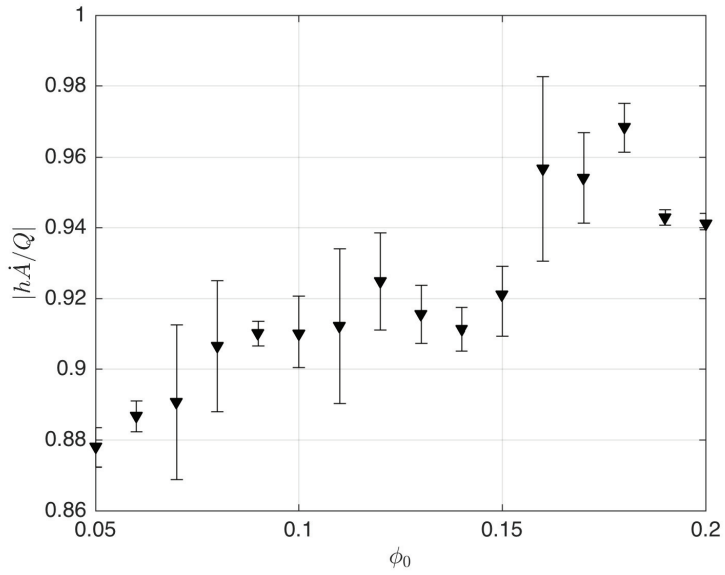

Figure 3.17: The plot shows the dimensionless rate of change of total suspension volume, $|h\dot{A}/Q|$, increases with ϕ_0

[192, 193]. This is in direct contrast with the behavior of a draining suspension, in which the increase in $\eta(\phi_0)$ increases the viscosity ratio between the suspension and invading air but clearly delays the onset of fingering. Further studies are required to elucidate the complex role of suspended particles to delay the start but to accelerate the inward fingering once it is formed.

3.3.3 Particle Drainage Versus Entrainment

Interestingly, the dimensionless time-rate of change of the suspension area, $|h\dot{A}/Q|$, increases with ϕ_0 as shown in the inset of Fig. 3.17. To explain this, we must consider how the suspension area relates to the amount of suspension that is left behind on the plate surfaces $V_{\rm p}$, or $A(t) = A(t=0) - [Qt + V_{\rm p}(t)]/h$. Hence, at given Q, the increase in $|\dot{A}|$ with ϕ_0 must result in the greater final volume of suspension left on the surface $V_{\rm p}(t_{\rm c})$, as confirmed by the plot of $V_{\rm p}^*(t_{\rm c}) = V_{\rm p}(t_{\rm c})/(t_{\rm c}Q)$ as a function of ϕ_0 in Fig. 3.18. This

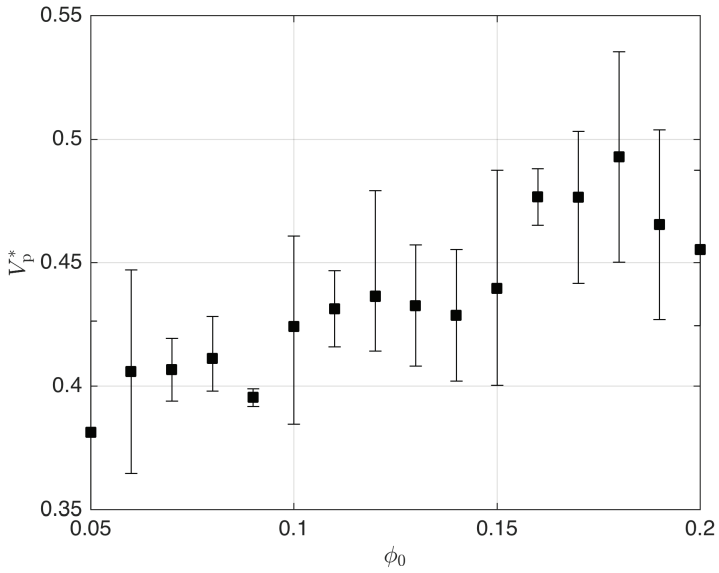

Figure 3.18: The normalized total volume of suspension left on the plate, $V_{\rm p}^*$, increases with ϕ_0 at $h = 1.39\,\mathrm{mm}$.

observation can be verified from the images took from the experiments shown in Fig. 3.19. When ϕ_0 is increasing, the particles left on the surface becomes more obvious and denser. In particular, at $\phi_0 = 0.2$, the final bulk suspension is surrounded by the layer of thin film of suspension on the plate.

Then, what causes some particles to be left behind on the plates, instead of draining into the well? As the air-suspension interface retracts towards the well, particles that become entrained into thin films of oil coating the plates will remain on the plate surfaces. Particle entrainment into thin films of viscous liquid has been previously studied in the context of dip coating of colloidal suspensions [194, 195, 196, 197, 188]. In particular, Colosqui and colleagues found that, as the plate is pulled from the bath of suspensions, particles entrain into the thin film only when they are small enough to fit inside the shear flow region near the plate, or $d < h_{\rm s}$, where $h_{\rm s}$ is the stagnation point on the meniscus relative to the plate. Here $h_{\rm s}$ separates the local shear flow from the bulk flow [188].

Figure 3.19: The amount of particles left on the surface is increasing when ϕ_0 increases from 0.05 to 0.2 observed from the experiments.

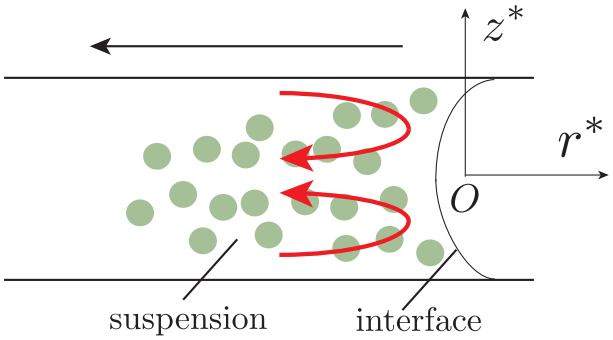

Figure 3.20: A schematic of the flow near the interface, where $z^* = z/h$ is normalized coordinate in the vertical direction and r^* is the normalized distance from the interface.

In the present experiments, there exists an analogous secondary flow (*i.e.* "fountain flow" [198]) downstream of the retracting interface, that can be described by the following stream function ψ [199]:

$$\psi = -\frac{Qz^*}{4\pi}\left(1-4z^{*2}\right)\left(1-\exp\left(r^*\sqrt{6}\right)\right), \tag{3.3}$$

where $z^* = z/h$ is the dimensionless vertical coordinate, while r^* corresponds to the dimensionless radial coordinate defined from the interface (see the schematic in Fig. 3.20). According to Bhattacherji et al. [199], when the interface in between two parallel plates is receding , the flow in the center region is in the same direction with the moving interface. However, the flow near the wall is flowing at an opposite direction to the flow in the center. Note that ψ neglects the effects of particles on the flow itself but qualitatively captures key flow characteristics near the interface. The corresponding streamlines in Fig. 3.21(a) reveal the flow reversal near the wall that may redirect particles towards the meniscus. To quantify the characteristic size of this reverse flow region, the dimensionless radial component of velocity, $u_{\mathrm{r}}/\bar{u}$, is computed based on $u_{\mathrm{r}} = -(1/r)(\partial\psi/\partial r)$,

$$u_{\mathrm{r}}/\bar{u} = \frac{1}{2}\left(1-12z^{*2}\right)\left(1-\exp\left(\sqrt{6}r^*\right)\right) \tag{3.4}$$

where $\bar{u}$ is the mean velocity of the interface.

As shown in Fig. 3.21(b), the distance from the wall, h_{s}, at which $u_{\mathrm{r}} = 0$ corresponds to $h/4.7$ and separates the back flow towards the meniscus (*i.e.* $u_{\mathrm{r}}/\bar{u} < 0$) from the draining flow (*i.e.* $u_{\mathrm{r}}/\bar{u} > 0$). Hence, particles whose diameter d is less than h_{s} are likely to be trapped in the meniscus and entrained into thin wetting films on the plates.

Consistent with the entrainment criterion of $d < h_{\mathrm{s}} \approx h/4.7$, the resultant amount of particles that remains on the plates must strongly depend on the value of h/d. This

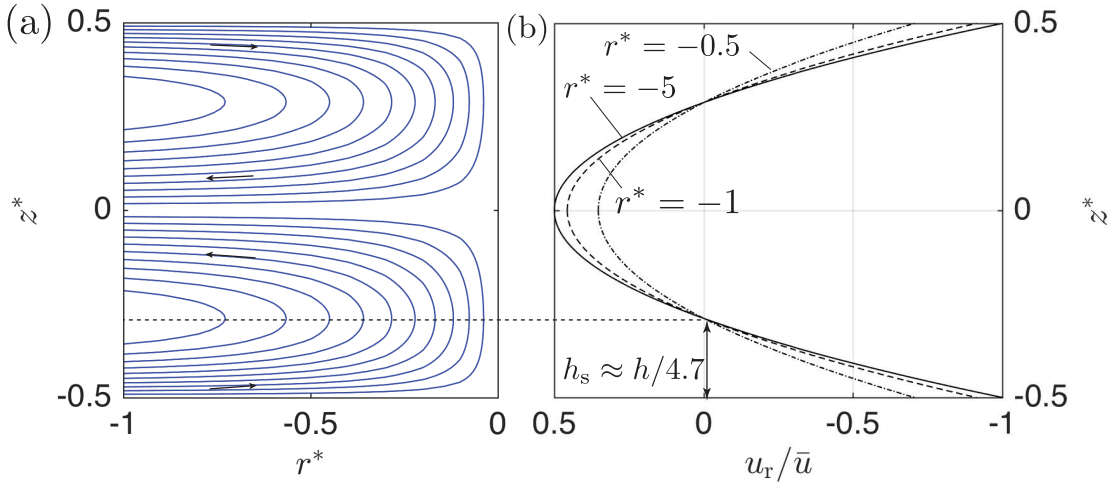

Figure 3.21: (a) The plot of streamlines of the fountain flow near the interface based on the simplified analytic solution. (b) Normalized radial velocity, $u_r/\bar{u}$, is plotted as a function of $z^* = z/h$ at various values of r^* from the interface. The distance from the wall at which $u_r = 0$ is computed to be $h_s \approx h/4.7$.

dependency of V_p^* on h/d at $\phi_0 = 0.05$, 0.1, and 0.2 is shown in Fig. 3.22 . Notably, V_p^* exhibits a steep drop and approaches zero when h/d is lowered from 6 to 4, independent of ϕ_0; V_p^*-dependency on ϕ_0 is observed only at large h/d, as the value of V_p^* diverges with varying ϕ_0. This transition in V_p^* is further corroborated by the experimental images at t_c for h/d = 3.8, 6.1 and 11.2 in Fig. 3.23. For h/d = 6.1 and 11.2 (*i.e.* $h/d > 4.7$) with $d = 125\,\mu$m, the final suspension is surrounded by a clear region of particles left on the plate surfaces, but the amount of entrained particles is substantially reduced at $h/d =$ 6.1. When h/d = 3.8 (*i.e.* $h/d < 4.7$) with larger particles where $d = 300\,\mu$m, almost no particles are observed on the plates, except close to the sink, which agrees well with the entrainment criterion.

3.4 Conclusions

In summary, we experimentally investigate the effect of neutrally buoyant particles on the interfacial dynamics of a draining suspension and its influence on the oil recovery

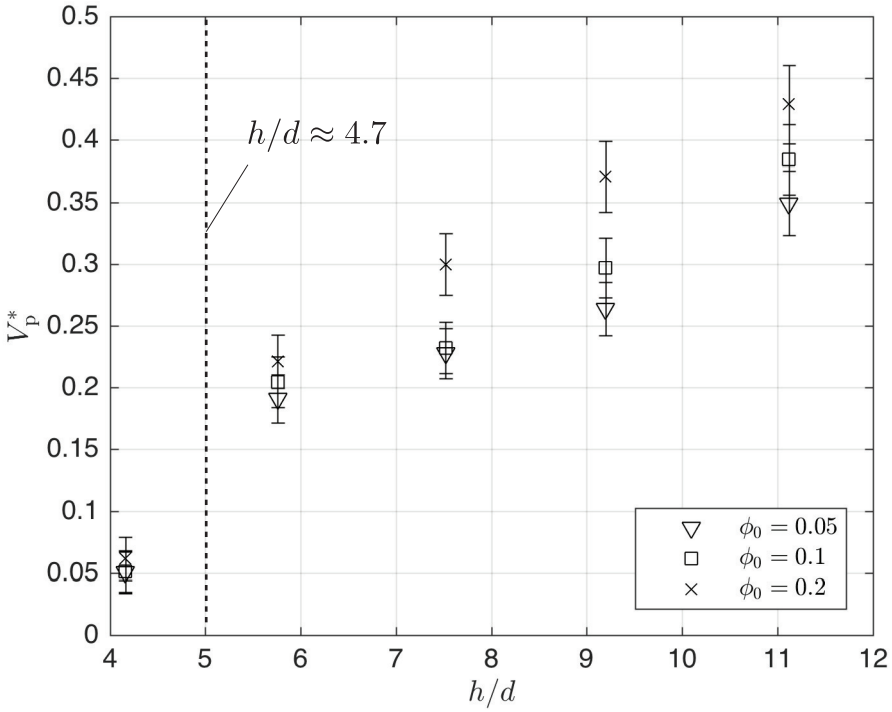

Figure 3.22: The plot of V_{p}^* versus h/d for $\phi_0 = 0.05$, 0.1, and 0.2 shows that V_{p}^* strongly depends on the channel gap thickness, h, relative to the particle diameter, d, at $Q = 7.5\,\mathrm{ml/min}$.

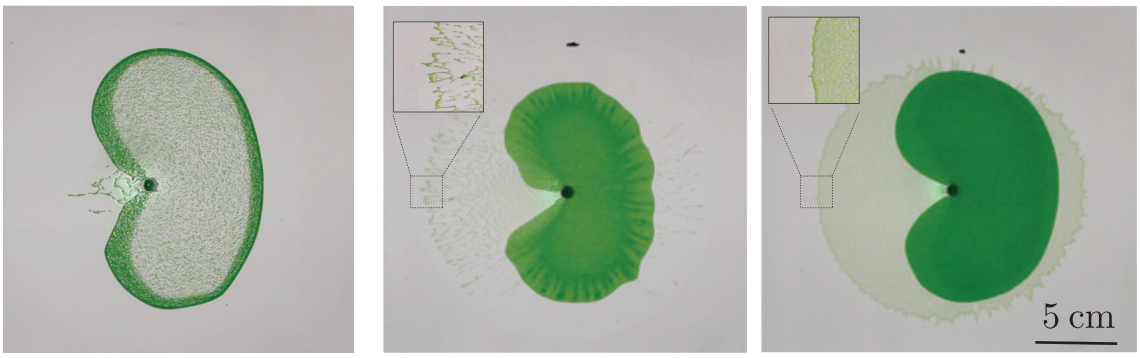

$h/d = 3.8$ $h/d = 6.1$ $h/d = 11.2$

Figure 3.23: Images of the suspension withdrawn at $Q = 7.5\,\mathrm{ml/min}$, for $h/d = 3.8$, 6.1 and 11.2, upon completion. The reduction in the amount of particles left on the plates with decreasing h/d is clearly demonstrated in the images.

efficiency. Our results show that the dominant finger grows and reaches the well faster with higher ϕ_0 that corresponds to an increase in the effective capillary number, Ca. This result qualitatively agrees with the numerical simulations by Kelly and Hinch [190] who predicted faster finger growth with Ca for a draining fluid. Despite the increase in the fingertip speed, we find that the total time of drainage and the total volume of suspension recovered also increase when more particles are added. Hence, the addition of particles can enhance the recovery efficiency of the suspension. In addition, particle entrainment into the thin film of oil causes some particles not to drain but to remain on the plates, giving rise to non-zero V_{p}^*, or the volume of suspension left on the plates. Based on an analytic solution of "fountain flow" downstream of the retracting interface [199, 198], we derive the particle entrainment criterion to be $d < h_{\mathrm{s}} \approx h/4.7$, which closely matches the experimental results. In turn, the amount of V_{p}^* directly influences the speed of the retracting interface, as $|h\dot{A}/Q|$ is found to increase with V_{p}^* and, thereby, ϕ_0.

Overall, understanding the effects of suspended particles on fluid-fluid interfaces applies to diverse engineering processes that go beyond oil recovery. In particular, aspects of the current research (*i.e.* particle entrainment) are directly relevant to the dip coating with suspensions [194, 195, 196, 197, 188], evaporation of complex drops, such as blood [200], that yield coffee-ring effects [201], and even nanoparticle printing [202, 203]. However, despite the growing interest in the interfacial dynamics of suspensions, many unanswered questions persist, and the continuum level description of suspensions appears to fall short. For instance, only one finger is observed in our experiment while Paterson observed multiple fingers [44] as the capillary number in his experiment is greater than ours. However, the critical capillary number below which there is only one finger is still unclear. Also, the equations derived by Paterson to predict the number of fingers and critical wavelength of the finger do not match our experimental results, which may be caused by the presence of particles. More experimental work and quantitative study may be required to solve

these issues. Another question is that the counterintuitive correlation between the drainage time and fingertip speed in the present study indicates that the onset of fingering must be delayed with increasing ϕ_0. The delay in fingering onset cannot be explained with the increasing effective viscosity ratio between the suspension and air alone (*i.e.* $\eta(\phi_0)/\eta_{\text{air}}$), as fingering initiates sooner with the increasing viscosity ratio in the pure liquid case [192, 193]. The effect of particles to delay the onset of fingering yet to accelerate it upon formation may require considering the "discrete" nature of particle-laden flows that separates them from their liquid counterpart and remains the topic of future investigation.

4. CONCLUSIONS AND FUTURE WORKS

4.1 Conclusions

In summary, the main objective of this Ph.D. work is to gain fundamental understanding of the coupled dynamics between particles and fluid-fluid interfaces, via experiments and reduced mathematical modeling. To achieve this goal, two different projects are involved, which consist of the single particle and multiple particles cases.

In the case of a single particle, we quantitatively study the oscillation bubble for particle trapping. The purpose of this research is to quantify the ability of bubbles to trap the particles depending on the bubble oscillation amplitude and acoustic parameters. Our collaborator from WSU perform the experiments and take the videos using a high-speed camera for particle trapping and single bubble oscillation. We use MATLAB to perform the image processing and data analysis. Once we collect the results from the experiments, we combine different theories to obtain a reduced mathematical model and find the critical acoustic parameters for particle trapping. We first apply the force balance on a single particle captured at the stagnation point of the bubble to calculate the critical secondary radiation force. Using Nyborg's equation, we compute the oscillation amplitude of the bubble to provide the critical radiation force. Then a linearized Rayleigh-Plesset equation is obtained to solve for the critical pressure in the microchannel. Finally, we solve the reduced Helmholtz equation with appropriate boundary conditions to find the threshold voltage. The prediction from our model agrees well with the experimental results. The quantitative results and reduced model in this research may potentially help the design of next-generation acoustic-based lab-on-a-chip devices for biological and medical applications.

The second research project involves multiple particles, where we study the viscous

fingering in a draining suspension. The objective of this project is to find how particle volume fraction in the suspension affects the growth rate of the viscous fingering and total drainage time. We perform experiments by draining the suspension from the Hele-Shaw cell with initial concentration from $0.05 - 0.2$ at various pump flow rate. The motion of the suspension is recorded and processed to find the fingering growth rate, the total time of drainage, and time of fingering onset. Our results show that the finger grows faster when adding more particles into the suspension. Surprisingly, the total time of drainage also increases with the particle volume fraction. The only reason that causes increasing of drainage time is the delayed onset of fingering at higher particle volume fraction, which is verified by our experimental results. Since the total volume of suspension recovered is strongly dependent on the total time of drainage, therefore adding more particles will increase the efficiency of the drainage. This result can, therefore, be helpful in many industry environmental applications such as the surface cleaning, 3D printing, and food processing. Another unexpected result is the observation of particles that are left on the surface of the plate during the drainage process. The amount of those particles increases when the gap thickness between the plates decreases. Inspired by the research from Colosqui et al. [188] and Karnis et al. [198], we can find an entrainment criteria for the suspension. If the particle size is smaller than a critical distance away from the plate, they are entrained into the thin film on the plate. We apply the stream function from Bhattacharji et al. [199] into our setup and derive the velocity profile. Finally, we calculate a critical distance in our system, which agrees well with the experiment results. The result of this research is essential to some manufacture or microfabrication processes such as dip coating or microstructure pattern formation.

4.2 Future Works

Since our models are derived based on various assumptions, there are still limitations and challenges in our current work. In the project of acoustic bubble, the external flow rate in the microchannel is limited over a certain value. When the bubble oscillates, it generates microstreaming in the nearby field. The microstreaming will induce a drag force on the particles, which can also affect the critical voltage for particle trapping. Our current model assumes that the external flow rate in the microchannel is strong enough so that we can neglect the microstreaming effect. However, in some practical situations, the external flow rate might be so small that the microstreaming drag force is dominant over the secondary radiation force. Also, when we consider the force balance for a captured particle at the stagnation point, there exists another possible force, such as the Saffman lift force, which may also affect the trapping of the particle. Future work for our current model will consider the effect of drag force from the microstreaming as well as the effect of lift force, and find the threshold external flow rate for the transition between the secondary radiation force and microstreaming drag force. For the experimental part, we can use a wider range of sizes for particles and bubbles to help the verification of our model. Another extension of our work is to include multiple particles or consider non-spherical, elastic objects, which is more relevant to biological applications such as manipulating blood cells or other microorganisms. Also, we currently extract the pressure inside the channel from the mathematical equations instead of direct measurement, which is lacking accuracy. To get a more precise value of pressure, we can use PIV (Particle Image Velocimetry) or a hydrophone for direct measurement in the future work.

In the draining suspension project, our current results indicate that the fingering onset is delayed by increasing the particle volume fraction, but the mechanism behind this observation is still unclear. The increase of effective viscosity cannot explain the delay of

fingering onset. Future work requires understanding the behavior of the particles inside the suspension. For instance, we need to study the theoretical equations which govern the particle migration. Second, our current pump suction flow rate is limited below $10\,\mathrm{ml/min}$. In fact, at a higher flow rate, which results in a higher capillary number, more fingers can be observed [190, 44]. However, the relation between the number of fingers and the value of capillary number still remains unknown, especially when particles are involved. One future work can include increasing the pump flow rate and change the gap thickness until multiple fingers can be observed, and quantitatively study how the increase of capillary number can affect the number of fingers. A mathematical model may also be obtained to predict the number of fingers with various parameters. Next, the current stream function of the fountain flow near the interface assumes flow without particles; therefore the velocity profile may not be so accurate to describe the actual motion of the particles near the interface. An extension of this work could include the effect of the particles into the fountain flow equation near the interface to derive a more sophisticated mathematical model for predicting the entrainment criteria. Lastly, from our experimental results, due to miscible fingering, we also observe a different layer of suspension inside the bulk suspension during drainage. Miscible fingering occurs due to the inhomogeneous distribution and gradient of particle volume fraction in the suspension. It is still unclear how miscible fingering will affect the drainage process, and how they are related to the capillary number. Hence, we can perform more experiments to quantitatively study the behavior of the miscible fingering and perform stability analysis to find the criteria of the finger growth.

REFERENCES

[1] D.-G. Lee and H.-Y. Kim, "Impact of superhydrophobic sphere onto water," *Langmuir*, vol. 24, pp. 142–145, November 2007.

[2] S. Poulain, G. Guenoun, S. Gart, W. Crowe, and S. Jung, "Particle motion induced by bubble cavitation," *Physical Review Letters*, vol. 114, p. 214501, May 2015.

[3] P. Zhang, J. M. Mines, S. Lee, and S. Jung, "Particle-bubble interaction inside a hele-shaw cell," *Physical Review E*, vol. 94, p. 023112, August 2016.

[4] L. A. Lubbers, Q. Xu, S. Wilken, W. W. Zhang, and H. M. Jaeger, "Dense suspension splat: Monolayer spreading and hole formation after impact," *Physical Review Letters*, vol. 113, p. 044502, July 2014.

[5] M. Trojer, M. L. Szulczewski, and R. Juanes, "Stabilizing fluid-fluid displacements in porous media through wettability alteration," *Physical Review Applied*, vol. 3, p. 054008, May 2015.

[6] X. Ding, S.-C. S. Lin, M. I. Lapsley, S. Li, X. Guo, C. Y. Chan, I.-K. Chiang, L. Wang, J. P. McCoy, and T. J. Huang, "Standing surface acoustic wave (SSAW) based multichannel cell sorting," *Lab on a Chip*, vol. 12, pp. 4228–4231, November 2012.

[7] Y. Xu, A. Hashmi, G. Yu, X. Lu, H.-J. Kwon, X. Chen, and J. Xu, "Microbubble array for on-chip worm processing," *Applied Physics Letters*, vol. 102, p. 023702, January 2013.

[8] S. K. Chung, Y. Zhao, U.-c. Yi, S. K. Cho, and L. Angeles, "Micro Bubble Fluidics by EWOD and Ultrasonic Excitation for Micro Bubble Tweezers," in *IEEE 20th In-*

ternational Conference on Micro Electro Mechanical Systems, Hyogo, Japan, January 21-25, 2007.

[9] S. K. Chung and S. K. Cho, "On-chip manipulation of objects using mobile oscillating bubbles," *Journal of Micromechanics and Microengineering*, vol. 18, p. 125024, December 2008.

[10] T. Tandiono, S. W. Ohl, D. S. Ow, E. Klaseboer, V. V. Wong, R. Dumke, and C. D. Ohl, "Sonochemistry and sonoluminescence in microfluidics," *Proceedings of the National Academy of Sciences*, vol. 108, pp. 5996–5998, April 2011.

[11] M. Böttner and C. Lang, *Recombinant Gene Expression*, ch. High-throughput expression in microplate format in Pichia Pastoris. Humana Press, 2004.

[12] B. Alberts, A. Johnson, J. Lewis, M. Raff, K. Roberts, and P. Walter, *Molecular biology of the cell*. Garland Science, 2002.

[13] H. Lodish, A. Berk, S. Zipursky, P. Matsudaura, D. Baltimore, and J. Darnell, *Molecular cell biology*. Freeman W.H. Company, 1999.

[14] W. Nyborg, "Radiation pressure on a small rigid sphere," *The Journal of Acoustical Society of America*, vol. 42, pp. 947–952, 1967.

[15] P. Marmottant and S. Hilgenfeldt, "Controlled vesicle deformation and lysis by single oscillating bubbles," *Nature*, vol. 423, pp. 153–156, May 2003.

[16] P. Marmottant, T. Biben, and S. Hilgenfeldt, "Deformation and rupture of lipid vesicles in the strong shear flow generated by ultrasound-driven microbubbles," *Proceedings of the Royal Society A: Mathematical, Physical and Engineering Sciences*, vol. 464, pp. 1781–1800, July 2008.

[17] J. Rooney, "Hemolysis near an ultrasonically pulsating gas bubble," *Science*, vol. 169, pp. 869–871, August 1970.

[18] M. W. Miller, D. L. Miller, and A. A. Brayman, "A review of in vitro bioeffects of inertial ultrasonic cavitation from a mehcanistic perspective," *Ultrasound in Medicine Biology*, vol. 22, no. 9, pp. 1131–1154, 1996.

[19] A. van Wamel, K. Kooiman, M. Harteveld, M. Emmer, F. ten Cate, M. Versluis, and N. de Jong, "Vibrating microbubbles poking individual cells: drug transfer into cells via sonoporation," *Journal of Control Release*, vol. 112, pp. 149–155, March 2006.

[20] M. Forbes, R. Steinberg, and W. O'Brein, "Examination of inertial cavitation of optison in producing sonoporation of chinese hamster ovary cells," *Ultrasound in Medicine Biology*, vol. 34, pp. 2009–2018, August 2008.

[21] N. Bose, D. Carugo, T. Maiti, X. Zhang, and S. Chakraborty, "The role of cell membrane strain in sonoporation characterised by microfluidic-based single-cell analysis," in *15th International Conference on Miniaturized System for Chemistry and Life Science*, Seatle, Washington, USA, October 2-6, 2011.

[22] S. M. Nejad, H. R. Hosseini, H. Akiyama, and K. Tachibana, "Optical observation of cell sonoporation with low intensity ultrasound," *Biochem Biophysics Research Communications*, vol. 413, pp. 218–223, September 2011.

[23] H. Vos, B. Dollet, M. Versluis, and N. de Jong, "Nonspherical shape oscillation of coated microbubbles in contact with a wall," *Ultrasound in Medicine Biology*, vol. 37, pp. 935–948, June 2011.

[24] Y. Qiu, C. Zhang, J. Tu, and D. Zhang, "Microbubble-induced sonoporation involved in ultrasound-mediated dna transfection in vitro at low acoustic pressures," *Journal of Biomechanics*, vol. 45, pp. 1339–1345, May 2009.

[25] W. Pitt, G. Husseini, and B. Staples, "Ultrasonic drug delivery-a general review," *Expert Opinion on Drug Delivery*, vol. 1, pp. 37–56, November 2004.

[26] W. Nyborg, "Biological effects of ultrasound: development of safety guidlines part ii: General review," *Ultrasound in Medicine Biology*, vol. 27, pp. 301–333, March 2001.

[27] K. Ferrara, M. Borden, and H. Zhang, "Lipid-shelled vehicles: engineering for ultrasound molecular imaging and drug delivery," *Accounts of Chemical Research*, vol. 42, pp. 881–892, June 2009.

[28] N. Rapoport, A. Kennedy, J. Shea, C. Scaife, and K. H. Nam, "Controlled and targeted tumor chemotherapy by ultrasound-activated nanoemulsions/microbubbles," *Journal of Control Release*, vol. 138, pp. 268–276, September 2009.

[29] L. Mullin, L. Philips, and P. Dayton, "Nanoparticle delivery enhancement with acoustically activated microbubbles," *IEEE Transactions on Ultrasonics, Ferroelectrics and Frequency Control*, vol. 60, pp. 65–77, January 2013.

[30] J. Oh, Y. Kwon, K. Lee, W. Jeong, S. Chung, and K. Rhee, "Drug perfusion enhancement in tissue model by steady streaming induced by oscillating microbubbles," *Computers in Biolody and Medicine*, vol. 44, pp. 37–43, January 2014.

[31] R. Price, D. Skyba, S. Kaul, and T. Skalak, "Delivery of colloidal particles and red blood cells to tissue through microvessel ruptures created by targeted microbubble destruction with ultrasound," *Circulation*, vol. 98, pp. 1264–1267, September 1998.

[32] E. Unger, T. McCeery, R. Sweitzer, V. Caldwell, and Y. Wu, "Acoustically active lipospheres containing paclitaxel: a newtherapeutic ultrasound contrast agents," *Investigative Radiology*, vol. 33, pp. 886–892, December 1998.

[33] I. Lentacker, S. de Smedt, J. Demeester, V. van Marck, M. Bracke, and N. Sanders, "Lipoplex-loaded microbubbles for gene delivery: a trojan horse controlled by ultrasound," *Advanced Functional Materials*, vol. 17, pp. 1910–1916, July 2007.

[34] I. Lentacker, S. de Smedt, and N. Sanders, "Drug loaded micro bubble design for ultrasound triggered delivery," *Soft Matter*, vol. 5, pp. 2161–2170, April 2009.

[35] A. Shi, Y. Min, and M. Wan, "Flowing microbubble manipulation in blood vessel phantom using ultrasonic standing wave with stepwise frequency," *Applied Physics Letters*, vol. 103, p. 174105, October 2013.

[36] Y. Yamakoshi, "Trapping of low sensitivity object by seed bubbles," in *IEEE Ultrasonics Symposium*, Rotterdam, Netherlands, September 18-21, 2005.

[37] C. Teupe, S. Richter, B. Fisslthaler, V. Randriamboavonjy, C. Ihling, I. Fleming, R. Busse, A. M. Zeiher, and S. Dimmeler, "Vascular gene transfer of phorphomimetic endothelial nitric oxide synthase using ultrasound-enhanced destruction of plasmid-loaded microbubbles improves vasoreactivity," *Circulation*, vol. 105, pp. 1104–1109, March 2002.

[38] M. Vannan, T. McCreery, P. Li, Z. Han, E. Unger, B. Kuersten, E. Nabel, and S. Rajagopalan, "Ultrasound-mediated transfection of canine myocardium by intravenous administration of cationic microbubble-linked plasmid DNA," *Journal of the American Society of Echocardiography*, vol. 15, pp. 213–218, March 2002.

[39] M. Shortencarier, P. Dayton, S. Bloch, P. Schumann, T. Matsunaga, and K. Ferrara, "A method for the radiation-force localized drug delivery using gas-filled lipospheres," *IEEE Transactions on Ultrasonics, Ferroelectrics and Frequency Control*, vol. 51, pp. 822–831, July 2004.

[40] Y. Z. Zhao, H. D. Liang, X. G. Mei, and M. Halliwell, "Preparation, characterization and in vivo obervation of phospholipid-based gas filled microbubbles containing hirudin," *Ultrasound in Medicine Biology*, vol. 31, pp. 1237–1243, September 2005.

[41] A. Kheirolomoom, P. Dayton, A. Lum, E. Little, E. Paoli, H. Zheng, and K. Ferrara, "Acoustically-active microbubbles conjugated to liposomes: characterization of a proposed drug delivery vehicle," *Journal of Control Release*, vol. 118, pp. 275–284, December 2007.

[42] K. Ferrara, R. Pollard, and M. Borden, "Ultrasound microbubble contrast agents: fundamentals and application to gene and drug delivery," *Annual Review of Biomedical Engineering*, vol. 9, pp. 415–447, August 2007.

[43] Y. Negishi, Y. Tsunoda, Y. E.-T. Y. Oda, R. Suzuki, K. Maruyama, M. Yamamoto, and Y. Aramaki, "Local gene delivery system by bubble liposomes and ultrasound exposure into joint synovium," *Journal of Drug Delivery*, vol. 2011, p. 203986, March 2011.

[44] L. Paterson, "Radial fingering in a hele shaw cell," *Journal of Fluid Mech*, vol. 113, pp. 513–529, December 1981.

[45] H. Thome, M. Rabaud, V. Hakim, and Y. Couder, "The saffman-taylor instability: From the linear to the circular geometry," *Physics of Fluids*, vol. 1, pp. 224–240, October 1988.

[46] P. G. Saffman and S. G. Taylor, "The penetration of a fluid into a porous medium or hele-shaw cell containing a more viscous liquid," *Proceedings of the Royal Society of London Series A-Mathematical Physical and Engineering Sciences*, vol. 245, pp. 312–329, June 1958.

[47] A. Lindner, D. Derks, and M. Shelley, "Strech flow of thin layers of newtonian liquids: Fingering patterns and lifting forces," *Physics of Fluids*, vol. 17, p. 072107, July 2005.

[48] J. Nase, D. Derks, and A. Lindner, "Dynamic evolution of fingering patterns in a lifted hele-shaw cell," *Physics of Fluids*, vol. 23, p. 123101, December 2011.

[49] M. B. Amar and D. Bonn, "Fingering instabilities in adhesive failure," *Physica D*, vol. 209, pp. 1–16, September 2005.

[50] P. H. A. Anjos, E. O. Dias, L. Dias, and J. A. Miranda, "Adhesion force in fluids: Effects of fingering, wetting, and viscous normal stress," *Physical Review E*, vol. 91, p. 013003, January 2015.

[51] L. Chen, S. Lee, J. Choo, and E. Lee, "Continuous dynamic flow micropumps for microfluid manipulation," *Journal of Micromechanics and Microengineering*, vol. 18, p. 013001, December 2007.

[52] C.-Y. Chen and Y.-S. Huang, "Radial hele-shaw flow with suction: Fully nonlinear pattern formation," *Physical Review E*, vol. 89, p. 053006, May 2014.

[53] H.-G. Lee, J. S. Lowengrub, and J. Goodman, "Modeling pinchoff and reconnection in a hele-shaw cell. ii. analysis and simulation in the nonlinear regime," *Physics of Fluids*, vol. 14, pp. 514–545, January 2002.

[54] X. Chen, J. Wu, R. Ma, M. Hua, N. Koratkar, S. Yao, and Z. Wang, "Nanograssed Micropyramidal Architectures for Continuous Dropwise Condensation," *Advanced Functional Materials*, vol. 21, pp. 4617–4623, December 2011.

[55] P. Daripa, "Hydrodynamic stability of multi-layer hele-shaw flows," *Journal of Statistical Mechancis*, vol. 2008, p. 12005, December 2008.

[56] P. Daripa, "Studies on stability in three-layer hele-shaw flows," *Physics of Fluids*, vol. 20, p. 112101, September 2008.

[57] P. Daripa and G. Pasa, "On capillary slowdown of viscous fingering in immiscible displacement in porous media," *Transport in Porous Media*, vol. 75, pp. 1–16, October 2008.

[58] P. Daripa and H. J. Hwang, "Nonlinear instability of hele-shaw flows with smooth viscous profiles," *Journal of Differential Equations*, vol. 245, pp. 1819–1837, October 2008.

[59] C. Gin and P. Daripa, "Stability results for multi-layer radial hele-shaw and porous media flows," *Physics of Fluids*, vol. 27, p. 012101, January 2015.

[60] P. Daripa and C. Gin, "Studies on dispersive stabilization of porous media flows," *Physics of Fluids*, vol. 28, p. 082105, August 2016.

[61] L. Cumings and J. R. King, "Hele-shaw flow with a point sink: generic soltion breakdown," *European Journal of Applied Mathematics*, vol. 15, pp. 1–37, February 2004.

[62] Q. Nie and F. R. Tian, "Singularities in hele-shaw flows," *SIAM Journal on Mathematical Analysis*, vol. 58, pp. 34–54, February 1998.

[63] Q. Nie and F. R. Tian, "Singularities in hele-shaw flows driven by a multipole," *SIAM Journal on Mathematical Analysis*, vol. 62, pp. 385–406, October 2001.

[64] E. D. Kelly and E. J. Hinch, "Numerical simulations of sink flow in the hele-shaw cell with small surface tension," *European Journal of Applied Mathematics*, vol. 8, pp. 533–550, December 1997.

[65] H. D. Ceniceros, T. Y. Hou, and H. Si, "Numerical study of hele-shaw flow with suction," *Physics of Fluids*, vol. 11, pp. 2471–2486, August 1999.

[66] K. J. Måløy, L. Furuberg, J. Feder, and T. Jøssang, "Dynamics of slow drainage in porous media," *Physical Review Letters*, vol. 68, pp. 2161–2164, April 1992.

[67] H. Auradou, K. J. Måløy, J. Schmittbuhl, A. Hansen, and D. Bideau, "Competition between correlated buoyancu and uncorrelated capillary effects during drainage," *Physical Review E*, vol. 60, pp. 7224–7234, December 1999.

[68] G. Løvoll, Y. Meheust, K. J. Måløy, E. Aker, and J. Schmittbuhl, "Competition of gravity, capillary and viscous forces during drainage in a two-dimensional porous medium, a pore scale study," *Energy*, vol. 30, pp. 861–872, May 2005.

[69] R. Toussaint, G. Løvoll, Y. Meheust, K. J. Måløy, and J. Schmittbuhl, "Influence of pore-scale disorder on visous fingering during drainage," *Europhysics Letters*, vol. 71, pp. 583–589, July 2005.

[70] O. Aursjø, G. Løvoll, H. A. Knudsen, E. G. Flekkøy, and K. J. Måløy, "A direct comparison between a slow pore scale drainage experiment and a 2d lattice boltzmann simulation," *Transport in Porous Media*, vol. 86, pp. 125–134, January 2011.

[71] B. Sandnes, E. Flekkøy, H. Knudsen, K. J. Måløy, and H. See, "Patterns and flow in frictional fluid dynamics," *Nature Communications*, vol. 2, no. 288, pp. 1–8, 2011.

[72] A. Islam, S. Chevalier, I. B. Salem, Y. Bernabe, R. Juanes, and M. Sassi, "Characterization of the crossover from capillary invasion to viscous fingering to fracturing during drainage in a vertical 2D porous medium," *International Journal of Multiphase Flow*, vol. 58, pp. 279–291, January 2014.

[73] G. M. Whitesides, "The origins and the future of microfluidics," *Nature*, vol. 442, pp. 368–373, July 2006.

[74] H. Stone, A. Stroock, and A. Ajdari, "Engineering Flows in Small Devices: Microfluidics Towards a Lab-on-a-Chip," *Annual Review of Fluid Mechanics*, vol. 36,

pp. 381–411, January 2004.

[75] D. Figeys and D. Pinto, "Lab-on-a-Chip: A Revolution in Biological and Medical Sciences," *Analytical Chemistry*, vol. 72, pp. 330–335, May 2000.

[76] S. Haeberle and R. Zengerle, "Microfluidic platforms for lab-on-a-chip applications," *Lab on a Chip*, vol. 7, pp. 1094–1110, September 2007.

[77] K.-i. Ohno, K. Tachikawa, and A. Manz, "Microfluidics: applications for analytical purposes in chemistry and biochemistry," *Electrophoresis*, vol. 29, pp. 4443–4453, November 2008.

[78] D. B. Weibel and G. M. Whitesides, "Applications of microfluidics in chemical biology," *Current Opinion in Chemical Biology*, vol. 10, pp. 584–591, December 2006.

[79] D. J. Beebe, G. Mensing, and G. M. Walker, "Physics and applications of microfluidics in biology," *Annual Review of Biomedical Engineering*, vol. 4, pp. 261–286, January 2002.

[80] J. Wang, L. Ren, L. Li, W. Liu, J. Zhou, W. Yu, D. Tong, and S. Chen, "Microfluidics: a new cosset for neurobiology," *Lab on a Chip*, vol. 9, pp. 644–652, March 2009.

[81] J. Pihl, M. Karlsson, and D. T. Chiu, "Microfluidic technologies in drug discovery," *Drug Discovery Today*, vol. 10, pp. 1377–1383, October 2005.

[82] P. S. Dittrich and A. Manz, "Lab-on-a-chip: microfluidics in drug discovery," *Nature Reviews: Drug Discovery*, vol. 5, pp. 210–218, March 2006.

[83] R. Barry and D. Ivanov, "Microfluidics in biotechnology," *Journal of Nanobiotechnology*, vol. 2, p. 2, March 2004.

[84] L. Guo, J. Feng, Z. Fang, J. Xu, and X. Lu, “Application of microfluidic "lab-on-a-chip" for the detection of mycotoxins in foods,” *Trends in Food Science & Technology*, vol. 46, pp. 252–263, December 2015.

[85] L. Marle and G. M. Greenway, “Microfluidic devices for environmental monitoring,” *Trends in Analytical Chemistry*, vol. 24, pp. 795–802, October 2005.

[86] J. Voldman, “Electrical forces for microscale cell manipulation,” *Annual Review of Biomedical Engineering*, vol. 8, pp. 425–454, January 2006.

[87] D. Kohlheyer, J. C. T. Eijkel, A. van den Berg, and R. B. M. Schasfoort, “Miniaturizing free-flow electrophoresis - a critical review,” *Electrophoresis*, vol. 29, pp. 977–993, March 2008.

[88] M. Dürr, J. Kentsch, T. Müller, T. Schnelle, and M. Stelzle, “Microdevices for manipulation and accumulation of micro- and nanoparticles by dielectrophoresis,” *Electrophoresis*, vol. 24, pp. 722–731, February 2003.

[89] P. Li, N. Lei, J. Xu, and W. Xue, “High-Yield Fabrication of Graphene Chemiresistors With Dielectrophoresis,” *IEEE Transactions on Nanotechnology*, vol. 11, pp. 751–759, July 2012.

[90] H. Shafiee, J. L. Caldwell, M. B. Sano, and R. V. Davalos, “Contactless dielectrophoresis: a new technique for cell manipulation,” *Biomedical Microdevices*, vol. 11, pp. 997–1006, October 2009.

[91] K. H. Kang, Y. Kang, X. Xuan, and D. Li, “Continuous separation of microparticles by size with direct current-dielectrophoresis,” *Electrophoresis*, vol. 27, pp. 694–702, February 2006.

[92] N. Pamme, J. C. Eijkel, and A. Manz, “On-chip free-flow magnetophoresis: Separation and detection of mixtures of magnetic particles in continuous flow,” *Journal*

of Magnetism and Magnetic Materials, vol. 307, pp. 237–244, December 2006.

[93] H. H. Bau, J. Zhong, and M. Yi, "A minute magneto hydro dynamic (MHD) mixer," *Sensors and Actuators B: Chemical*, vol. 79, pp. 207–215, October 2001.

[94] M. A. M. Gijs, "Magnetic bead handling on-chip: new opportunities for analytical applications," *Microfluidics and Nanofluidics*, vol. 1, pp. 22–40, October 2004.

[95] T. Zhu, R. Cheng, Y. Liu, J. He, and L. Mao, "Combining positive and negative magnetophoreses to separate particles of different magnetic properties," *Microfluidics and Nanofluidics*, vol. 17, pp. 973–982, April 2014.

[96] M. Ozkan, M. Wang, C. Ozkan, R. Flynn, and S. Esener, "Optical manipulation of objects and biological cells in microfluidic devices," *Biomedical Microdevices*, vol. 5, pp. 61–67, March 2003.

[97] F. Arai, C. Ng, H. Maruyama, A. Ichikawa, H. El-Shimy, and T. Fukuda, "On chip single-cell separation and immobilization using optical tweezers and thermosensitive hydrogel," *Lab on a Chip*, vol. 5, pp. 1399–1403, December 2005.

[98] H. Zhang and K.-K. Liu, "Optical tweezers for single cells," *Journal of the Royal Society Interface*, vol. 5, pp. 671–690, July 2008.

[99] F. Gallaire, C. N. Baroud, J.-P. Delville, and Others, "Thermocapillary manipulation of microfluidic droplets: theory and applications," *International Journal of Heat and Technology*, vol. 26, pp. 161–166, May 2009.

[100] A. Darhuber, J. Valentino, S. Troian, and S. Wagner, "Thermocapillary actuation of droplets on chemically patterned surfaces by programmable microheater arrays," *Journal of Microelectromechanical Systems*, vol. 12, pp. 873–879, December 2003.

[101] R. D. Johnson, I. H. A. Badr, G. Barrett, S. Lai, Y. Lu, M. J. Madou, and L. G. Bachas, "Development of a Fully Integrated Analysis System for Ions Based on Ion-

Selective Optodes and Centrifugal Microfluidics," *Analytical Chemistry*, vol. 73, pp. 3940–3946, August 2001.

[102] R. Gorkin, J. Park, J. Siegrist, M. Amasia, B. S. Lee, J.-M. Park, J. Kim, H. Kim, M. Madou, and Y.-K. Cho, "Centrifugal microfluidics for biomedical applications," *Lab on a Chip*, vol. 10, pp. 1758–1773, July 2010.

[103] H. Bruus, J. Dual, J. Hawkes, M. Hill, T. Laurell, J. Nilsson, S. Radel, S. Sadhal, and M. Wiklund, "Forthcoming Lab on a Chip tutorial series on acoustofluidics: acoustofluidics-exploiting ultrasonic standing wave forces and acoustic streaming in microfluidic systems for cell and particle manipulation," *Lab on a Chip*, vol. 11, pp. 3579–3580, November 2011.

[104] J. Friend and L. Y. Yeo, "Microscale acoustofluidics: Microfluidics driven via acoustics and ultrasonics," *Reviews of Modern Physics*, vol. 83, pp. 647–704, June 2011.

[105] S.-C. S. Lin, X. Mao, and T. J. Huang, "Surface acoustic wave (SAW) acoustophoresis: now and beyond," *Lab on a Chip*, vol. 12, pp. 2766–2770, August 2012.

[106] L. Y. Yeo and J. R. Friend, "Ultrafast microfluidics using surface acoustic waves," *Biomicrofluidics*, vol. 3, p. 12002, January 2009.

[107] G. Yu, X. Chen, and J. Xu, "Acoustophoresis in variously shaped liquid droplets," *Soft Matter*, vol. 7, p. 10063, July 2012.

[108] A. Lenshof, C. Magnusson, and T. Laurell, "Acoustofluidics 8: applications of acoustophoresis in continuous flow microsystems," *Lab on a Chip*, vol. 12, pp. 1210–1223, April 2012.

[109] S. M. Hagsäter, T. G. Jensen, H. Bruus, and J. P. Kutter, "Acoustic resonances in microfluidic chips: full-image micro-PIV experiments and numerical simulations.,"

Lab on a Chip, vol. 7, pp. 1336–1344, October 2007.

[110] P.-H. Huang, Y. Xie, D. Ahmed, J. Rufo, N. Nama, Y. Chen, C. Y. Chan, and T. J. Huang, "An acoustofluidic micromixer based on oscillating sidewall sharp-edges," *Lab on a Chip*, vol. 13, pp. 3847–3852, October 2013.

[111] A. Hashmi, G. Yu, M. Reilly-Collette, G. Heiman, and J. Xu, "Oscillating bubbles: a versatile tool for lab on a chip applications," *Lab on a Chip*, vol. 12, pp. 4216–4227, November 2012.

[112] Y. Chen and S. Lee, "Manipulation of biological objects using acoustic bubbles: a review," *Integrative and Comparative Biology*, vol. 54, pp. 959–968, December 2014.

[113] W. Lauterborn and T. Kurz, "Physics of bubble oscillations," *Reports on Progress in Physics*, vol. 73, p. 106501, October 2010.

[114] B. Tran, T. Hall, J. Fowlkes, and C. Cain, "Microbubble-enhanced cavitation for noninvasive ultrasound surgery," *IEEE Transactions on Ultrasonics, Ferroelectrics and Frequency Control*, vol. 50, pp. 1296–1304, October 2003.

[115] Y. Liu, H. Yang, and A. Sakanishi, "Ultrasound: mechanical gene transfer into plant cells by sonoporation," *Biotechnology Advances*, vol. 24, pp. 1–16, June 2006.

[116] N. B. Smith, "Perspectives on transdermal ultrasound mediated drug delivery," *International Journal of Nanomedicine*, vol. 2, pp. 585–594, December 2007.

[117] W. D. O'Brien, "Ultrasound-biophysics mechanisms," *Progress in Biophysics and Molecular Biology*, vol. 93, pp. 212–255, September 2007.

[118] J. Xu and D. Attinger, "Acoustic excitation of superharmonic capillary waves on a meniscus in a planar microgeometry," *Physics of Fluids*, vol. 19, p. 108107, September 2007.

[119] D. Hsieh, "On thresholds for surface waves and subharmonics of an oscillating bubble," *The Journal of the Acoustical Society of America*, vol. 56, pp. 392–393, August 1974.

[120] S. A. Elder, "Cavitation Microstreaming," *The Journal of the Acoustical Society of America*, vol. 31, p. 54, January 1959.

[121] P. Tho, R. Manasseh, and A. Ooi, "Cavitation microstreaming patterns in single and multiple bubble systems," *Journal of Fluid Mechanics*, vol. 576, pp. 191–233, March 2007.

[122] J. Xu and D. Attinger, "Control and ultrasonic actuation of a gas–liquid interface in a microfluidic chip," *Journal of Micromechanics and Microengineering*, vol. 17, pp. 609–616, March 2007.

[123] L. A. Crum, "Bjerknes forces on bubbles in a stationary sound field," *The Journal of the Acoustical Society of America*, vol. 57, pp. 1363–1370, June 1975.

[124] P. Rogers and A. Neild, "Selective particle trapping using an oscillating microbubble," *Lab on a Chip*, vol. 11, pp. 3710–3715, November 2011.

[125] S. K. Chung and S. K. Cho, "3-D manipulation of millimeter- and micro-sized objects using an acoustically excited oscillating bubble," *Microfluidics and Nanofluidics*, vol. 6, pp. 261–265, July 2008.

[126] P. Marmottant and S. Hilgenfeldt, "A bubble-driven microfluidic transport element for bioengineering," *Proceedings of the National Academy of Sciences of the United States of America*, vol. 101, pp. 9523–9527, June 2004.

[127] P. Marmottant, M. Versluis, N. de Jong, S. Hilgenfeldt, and D. Lohse, "High-speed imaging of an ultrasound-driven bubble in contact with a wall: "Narcissus" effect

and resolved acoustic streaming," *Experiments in Fluids*, vol. 41, pp. 147–153, December 2005.

[128] Y. Xie, D. Ahmed, M. I. Lapsley, M. Lu, S. Li, and T. J. Huang, "Acoustofluidic relay: sequential trapping and transporting of microparticles via acoustically excited oscillating bubbles," *Journal of Laboratory Automation*, vol. 19, pp. 137–143, April 2014.

[129] A. Hashmi, G. Heiman, G. Yu, M. Lewis, H.-J. Kwon, and J. Xu, "Oscillating bubbles in teardrop cavities for microflow control," *Microfluidics and Nanofluidics*, vol. 14, pp. 591–596, October 2012.

[130] A. Ozcelik, D. Ahmed, Y. Xie, N. Nama, Z. Qu, A. A. Nawaz, and T. J. Huang, "An acoustofluidic micromixer via bubble inception and cavitation from microchannel sidewalls," *Analytical Chemistry*, vol. 86, pp. 5083–5088, May 2014.

[131] A. R. Tovar, M. V. Patel, and A. P. Lee, "Lateral air cavities for microfluidic pumping with the use of acoustic energy," *Microfluidics and Nanofluidics*, vol. 10, pp. 1269–1278, January 2011.

[132] A. R. Tovar and A. P. Lee, "Lateral cavity acoustic transducer," *Lab on a Chip*, vol. 9, pp. 41–43, January 2009.

[133] M. V. Patel, A. R. Tovar, and A. P. Lee, "Lateral cavity acoustic transducer as an on-chip cell/particle microfluidic switch," *Lab on a Chip*, vol. 12, pp. 139–145, January 2012.

[134] P.-H. Huang, M. Ian Lapsley, D. Ahmed, Y. Chen, L. Wang, and T. Jun Huang, "A single-layer, planar, optofluidic switch powered by acoustically driven, oscillating microbubbles," *Applied Physics Letters*, vol. 101, p. 141101, October 2012.

[135] J. Kao, X. Wang, J. Warren, J. Xu, and D. Attinger, "A bubble-powered micro-rotor: conception, manufacturing, assembly and characterization," *Journal of Micromechanics and Microengineering*, vol. 17, pp. 2454–2460, December 2007.

[136] D. Ahmed, C. Y. Chan, S.-C. S. Lin, H. S. Muddana, N. Nama, S. J. Benkovic, and T. J. Huang, "Tunable, pulsatile chemical gradient generation via acoustically driven oscillating bubbles," *Lab on a Chip*, vol. 13, pp. 328–331, February 2013.

[137] J. M. Won, J. H. Lee, K. H. Lee, K. Rhee, and S. K. Chung, "Propulsion of water-floating objects by acoustically oscillating microbubbles," *International Journal of Precision Engineering and Manufacturing*, vol. 12, pp. 577–580, June 2011.

[138] J. Feng and S. K. Cho, "Micro propulsion in liquid by oscillating bubbles," in *IEEE 26th International Conference on Micro Electro Mechanical Systems (MEMS)*, Taipei, Taiwan, January 20-24, 2013.

[139] S. Hagsater, A. Lenshof, P. Skafte-Pedersen, J. Kutter, T. Laurell, and H. Bruus, "Acoustic resonances in straight micro channels: Beyond the 1D-approximation," *Lab on a Chip*, vol. 8, pp. 1178–1184, May 2008.

[140] P. Marmottant and S. Hilgenfeldt, "Controlled vesicle deformation and lysis by single oscillating bubbles," *Nature*, vol. 423, pp. 153–156, May 2003.

[141] C. Wang, B. Rallabandi, and S. Hilgenfeldt, "Frequency dependence and frequency control of microbubble streaming flows," *Physics of Fluids*, vol. 25, p. 022002, February 2013.

[142] P. Marmottant and S. Hilgenfeldt, "A bubble-driven microfluidic transport element for bioengineering," *Proceedings of the National Academy of Sciences*, vol. 101, pp. 9523–9527, June 2004.

[143] P. Marmottant, J. Raven, H. Gardeniers, J. Bomer, and S. Hilgenfeldt, "Microfluidics with ultrasound-driven bubbles," *Journal of Fluid Mechanics*, vol. 568, pp. 109–118, December 2006.

[144] B. Rallabandi, C. Wang, and S. Hilgenfeldt, "Two-dimensional streaming flows driven by sessile semicylindrical microbubbles," *Journal of Fluid Mechanics*, vol. 739, pp. 57–71, January 2014.

[145] A. Doinikov and S. Zavtrak, "Interaction force between a bubble and a solid particle in a sound field," *Ultrasonic*, vol. 34, pp. 807–815, December 1996.

[146] P. Rogers and A. Neild, "Selective particle trapping using an oscillating microbubble," *Lab on a Chip*, vol. 11, pp. 3710–3715, November 2011.

[147] X. Huang, W. Hui, C. Hao, W. Yue, M. Yang, Y. Cui, and Z. Wang, "On-site formation of emulsions by controlled air plugs," *Small*, vol. 10, pp. 758–765, February 2014.

[148] S. L. Goren and M. E. O'Neill, "On the hydrodynamic resistance to a particle of a dilute suspension when in the neighbourhood of a large obstacle," *Chemical Engineering Science*, vol. 26, pp. 325 – 338, June 1970.

[149] M. P. Brenner, S. Hilgenfeldt, and D. Lohse, "Single-bubble sonoluminescence," *Reviews of Modern Physics*, vol. 74, pp. 425–484, May 2002.

[150] C. E. Brennen, *Cavitation and Bubble Dynamics*, ch. Spherical Bubble Dynamics. Cambridge University Press, 1995.

[151] H. Bruus, *Theoretical Microfluidics*, ch. Acustofluidics. Oxford University Press, 2008.

[152] B. W. van Oudheusden, "PIV-based pressure measurement," *Measurement Science and Technology*, vol. 24, p. 032001, January 2013.

[153] R. L. Chuoke, P. van Meurs, and C. van der Poel, "The instability of slow, immiscible, viscous liquid-liquid displacements in permeable media," *Petroleum Transaction*, vol. 216, pp. 188–194, 1959.

[154] P. G. Saffman, "Viscous fingering in a hele-shaw cell," *Journal of Fluid Mechanics*, vol. 173, pp. 73–94, December 1986.

[155] G. M. Homsy, "Viscous fingering in porous media," *Annual Review of Fluid Mechanics*, vol. 19, pp. 271–311, January 1987.

[156] D. Standnes and I. Skjevrak, "Literature review of implemented polymer field projects," *Journal of Petroleum Science and Engineering*, vol. 122, pp. 761 – 775, October 2014.

[157] C. T. Montgomery and M. B. Smith, "Hydraulic fracturing: History of an enduring technology," *Journal of Petroleum Technology*, vol. 62, pp. 26–32, December 2010.

[158] M. J. Economides, D. A. Hill, C. Ehlig-Economides, and D. Zhu, *Petroleum Production Systems*. Prentice Hall, 2nd ed., 2012.

[159] Y. Liu, P. B. Gadde, and M. M. Sharma, "Proppant placement using reverse-hybrid fracs," *SPE Production & Operations*, vol. 22, pp. 348–356, August 2007.

[160] S. Malhotra, E. R. Lehman, and M. M. Sharma, "Proppant placement using alternate-slug fracturing," in *SPE Hydraulic Fracturing Conference*, The Woodlands, TX, USA, February 4-6, 2013.

[161] H. D. Ceniceros, T. Y. Hou, and H. Si, "Numerical study of hele-shaw flow with suction," *Physics of Fluids*, vol. 11, pp. 2471–2486, August 1999.

[162] D. S. Pope, L. K.-W. Leung, J. Gulbis, and V. G. Constien, "Effects of viscous fingering on fracture conductivity," *SPE Production & Facilities*, vol. 11, pp. 230–237, November 1996.

[163] J. S. Andrews and H. Kjorholt, "Rock mechanical principles help to predict proppant flowback from hydraulic fractures," in *SPE/ISRM Rock Mechanics in Petroleum Engineering*, Trondheim, Norway, July 8-10, 1998.

[164] R. J. Furbank and J. F. Morris, "An experimental study of particle effects on drop formation," *Physics of Fluids*, vol. 16, pp. 1777–1790, April 2004.

[165] R. J. Furbank and J. F. Morris, "Pendant drop thread dynamics of particle-laden liquids," *International Journal of Multiphase Flow*, vol. 33, pp. 448 – 468, April 2007.

[166] C. Bonnoit, T. Bertrand, E. Clément, and A. Lindner, "Accelerated drop detachment in granular suspensions," *Physics of Fluids*, vol. 24, p. 043304, April 2012.

[167] T. Bertrand, C. Bonnoit, E. Clément, and A. Lindner, "Dynamics of drop formation in granular suspensions: the role of volume fraction," *Granular Matter*, vol. 14, pp. 169–174, April 2012.

[168] M. Z. Miskin and H. M. Jaeger, "Droplet formation and scaling in dense suspensions," *Proceedings of the National Academy of Sciences*, vol. 109, pp. 4389–4394, January 2012.

[169] M. van Deen, T. Bertrand, N. Vu, D. Quéré, E. Clément, and A. Lindner, "Particles accelerate the detachment of viscous liquids," *Rheologica Acta*, vol. 52, pp. 403–412, May 2013.

[170] B. P. Cook, "Theory for particle settling and shear-induced migration in thin-film liquid flow," *Physical Review E*, vol. 78, p. 045303, October 2008.

[171] J. Zhou, B. Dupuy, A. L. Bertozzi, and A. E. Hosoi, "Theory for shock dynamics in particle-laden thin films.," *Physical Review Letters*, vol. 94, p. 117803, March 2005.

[172] T. Ward, C. Wey, R. Glidden, A. E. Hosoi, and A. L. Bertozzi, "Experimental study of gravitation effects in the flow of a particle-laden film on an inclined plane," *Physics of Fluids*, vol. 21, p. 083305, August 2009.

[173] N. Murisic, J. Ho, V. Hu, P. Latterman, T. Koch, K. Lin, M. Mata, and A. L. Bertozzi, "Particle-laden viscous thin-film flows on an incline: experiments compared with an equilibrium theory based on shear-induced migration and particle settling," *Physica D*, vol. 240, pp. 1661–1673, October 2011.

[174] N. Murisic, B. Pausader, D. Peschka, and A. L. Bertozzi, "Dynamics of particle settling and resuspension in viscous liquid films," *Journal of Fluid Mechanics*, vol. 717, pp. 203–231, February 2013.

[175] A. Mavromoustaki and A. L. Bertozzi, "Hyperbolic systems of conservation laws in gravity-driven, particle-laden thin-film flows," *Journal of Engineering Mathematics*, vol. 88, pp. 29–48, October 2014.

[176] G. Wang, S. Zhou, J. Joshi, G. J. Jameson, and G. M. Evans, "An energy model on particle detachment in the turbulent field," *Minerals Engineering*, vol. 69, pp. 165–169, December 2014.

[177] S. Lee, Y. Stokes, and A. L. Bertozzi, "Behavior of a particle-laden flow in a spiral channel," *Physics of Fluids*, vol. 26, p. 043302, April 2014.

[178] S. Lee, J. Wong, and A. Bertozzi, "Equilibrium theory of bidensity particle-laden flows on an incline," in *Mathematical Modelling and Numerical Simulation of Oil Pollution Problems* (M. Ehrhardt, ed.), Springer, 2015.

[179] H. Tang, W. Grivas, D. Homentcovschi, J. Geer, and T. Singler, "Stability considerations associated with the meniscoid particle band at advancing interfaces in hele-

shaw suspension flows," *Physical Review Letters*, vol. 85, pp. 2112–2115, September 2000.

[180] A. Ramachandran and D. T. Leighton, "Particle migration in concentrated suspensions undergoing squeeze flow," *Journal of Rheology*, vol. 54, pp. 563–589, May 2010.

[181] F. Xu, J. Kim, and S. Lee, "Particle-induced viscous fingering," *Journal of Non-Newtonian Fluid Mechanics*, vol. 238, pp. 92–99, December 2016.

[182] J. Kim, F. Xu, and S. Lee, "Formation and destabilization of the particle band on the fluid-fluid interface," *Physical Review Letters*, vol. 118, p. 074501, February 2017.

[183] C. Chevalier, A. Lindner, and E. Clement, "Destabilization of a saffman-taylor fingerlike pattern in a granular suspension," *Physical Review Letters*, vol. 99, p. 174501, October 2007.

[184] Ø. Johnsen, C. Chevalier, A. Lindner, R. Toussaint, E. Clément, K. J. Måløy, E. G. Flekkøy, and J. Schmittbuhl, "Decompaction and fluidization of a saturated and confined granular medium by injection of a viscous liquid or gas," *Physical Review E*, vol. 78, p. 051302, November 2008.

[185] C. Chevalier, A. Lindner, M. Leroux, and E. Clément, "Morphodynamics during air injection into a confined granular suspension," *Journal of Non-Newtonian Fluid Mechanics*, vol. 158, pp. 63 – 72, May 2009.

[186] B. Sandnes, E. G. Flekkoy, H. A. Knudsen, K. J. Maloy, and H. See, "Patterns and flow in frictional fluid dynamics," *Nature Communications*, vol. 2, p. 288, April 2011.

[187] J. A. Eriksen, B. Marks, B. Sandnes, and R. Toussaint, "Bubbles breaking the wall: Two-dimensional stress and stability analysis," *Physical Review E*, vol. 91,

p. 052204, May 2015.

[188] C. E. Colosqui, J. F. Morris, and H. A. Stone, "Hydrodynamically driven colloidal assembly in dip coating," *Physical Review Letters*, vol. 110, p. 188302, May 2013.

[189] N. A. Bharadwaj and E. H. Randy, "Single-point parallel disk correction for asymptotically nonlinear oscillatory shear," *Rheologica Acta*, vol. 54, pp. 223–233, March 2015.

[190] E. D. Kelly and E. J. Hinch, "Numerical simulations of sink flow in the hele-shaw cell with small surface tension," *European Journal of Applied Mathematics*, vol. 8, pp. 533–550, December 1997.

[191] J. F. Morris and J. F. Brady, "Pressure-driven flow of a suspension: Buoyancy effects," *International Journal of Multiphase Flow*, vol. 24, pp. 105 – 130, February 1998.

[192] I. Bischofberger, R. Ramachandran, and S. R. Nagel, "Fingering versus stability in the limit of zero interfacial tension," *Nature Communications*, vol. 5, p. 5265, October 2014.

[193] I. Bischofberger, R. Ramachandran, and S. R. Nagel, "An island of stability in a sea of fingers: emergent global features of the viscous-flow instability," *Soft Matter*, vol. 11, pp. 7428–7432, October 2015.

[194] O. Giraldo, J. P. Durand, H. Ramanan, K. Laubernds, S. L. Suib, M. Tsapatsis, S. L. Brock, and M. Marquez, "Dynamic organization of inorganic nanoparticles into periodic micrometer-scale patterns," *Angewandte Chemie*, vol. 115, pp. 3011–3015, June 2003.

[195] M. Abkarian, J. Nunes, and H. A. Stone, "Colloidal crystallization and banding in a cylindrical geometry," *Journal of the American Chemical Society*, vol. 126,

pp. 5978–5979, April 2004.

[196] M. Ghosh, F. Fan, and K. J. Stebe, "Spontaneous pattern formation by dip coating of colloidal suspensions on homogeneous surfaces," *Langmuir*, vol. 23, pp. 2180–2183, January 2007.

[197] S. Watanabe, K. Inukai, S. Mizuta, and M. T. Miyahara, "Mechanism for stripe pattern formation on hydrophilic surfaces by using convective self-assembly," *Langmuir*, vol. 25, pp. 7287–7295, June 2009. PMID: 19492788.

[198] A. Karnis and S. Mason, "The flow of suspensions through tubes vi. meniscus effects," *Journal of Colloid and Interface Science*, vol. 23, pp. 120 – 133, January 1967.

[199] S. Bhattacharji and P. Savic, "Real and apparent non-newtonian behavior in viscous pipe flow of suspensions driven by a fluid piston," in *Proceedings of Heat Transfer and Fluid Mechanics Institute*, vol. 15, pp. 249–262, 1965.

[200] D. Brutin, B. Sobac, and C. Nicloux, "Influence of substrate nature on the evaporation of a sessile drop of blood," *Journal of Heat Transfer*, vol. 134, p. 061101, May 2012.

[201] R. D. Deegan, O. Bakajin, T. F. Dupont, G. Huber, S. R. Nagel, and T. A. Witten, "Capillary flow as the cause of ring stains from dried liquid drops," *Nature*, vol. 389, pp. 827–829, October 1997.

[202] B. G. Prevo and O. D. Velev, "Controlled, rapid deposition of structured coatings from micro- and nanoparticle suspensions," *Langmuir*, vol. 20, pp. 2099–2107, February 2004.

[203] T. Kraus, L. Malaquin, H. Schmid, W. Riess, N. D. Spencer, and H. Wolf, "Nanoparticle printing with single-particle resolution," *Nature Nanotechnology*,

vol. 2, pp. 570–576, September 2007.